

First-principles simulated-annealing study of phase transitions and short-range order in transition-metal and semiconductor alloys

Z. W. Lu,* D. B. Laks,† S.-H. Wei, and Alex Zunger
National Renewable Energy Laboratory, Golden, Colorado 80401
 (Received 3 May 1994)

Total-energy local-density calculations on approximately 20 periodic crystal structures of a given AB compound are used to define a long-range Ising Hamiltonian which correctly represents atomic relaxations. This allows us to accurately calculate structural energies of *relaxed* substitutional $A_{1-x}B_x$ systems containing thousands of transition-metal atoms, simply by adding up spin products in the Ising Hamiltonian. The computational cost is thus size independent. We then apply Monte Carlo and simulated-annealing techniques to this Ising Hamiltonian, finding (i) the $T = 0$ ground-state structures, (ii) the order-disorder transition temperatures T_c , and (iii) the $T > T_c$ short-range-order parameters. The method is illustrated for a transition-metal alloy ($\text{Cu}_{1-x}\text{Pd}_x$) and a semiconductor alloy ($\text{Ga}_{1-x}\text{In}_x\text{P}$). It extends the applicability of the local-density method to finite temperatures and to huge substitutional supercells. We find for $\text{Cu}_{0.75}\text{Pd}_{0.25}$ a characteristic fourfold splitting of the diffuse scattering intensity due to short-range order as observed experimentally.

I. INTRODUCTION

The cluster expansion¹ (CE) is a powerful method for extending the applicability of first-principles total-energy calculations to a large range of substitutional configurations. In the CE, a solid made up of A and B atoms is treated as a lattice problem, assigning a set of “spin” variables \hat{S}_i ($i = 1, 2, \dots, N$) to each of the N sites of the lattice, with $\hat{S}_i = -1$ if site i is occupied by an A atom, and $\hat{S}_i = +1$ if it is occupied by a B atom. A configuration σ is then defined by the occupation of each of the N lattice sites by an A atom or a B atom. The energies of any of the 2^N possible configurations σ can be *exactly*² mapped into a generalized Ising Hamiltonian:

$$E(\sigma) = J_0 + \sum_i J_i \hat{S}_i(\sigma) + \sum_{j < i} J_{ij} \hat{S}_i(\sigma) \hat{S}_j(\sigma) + \sum_{k < j < i} J_{ijk} \hat{S}_i(\sigma) \hat{S}_j(\sigma) \hat{S}_k(\sigma) + \dots, \quad (1)$$

where the J 's are “interaction energies,” and the first summation is over all sites in the lattice, the second over all pairs of sites, the third over all triplets, and so on. The interaction energies J are the same for all configurations σ . Thus, if the J 's can be calculated and if the series [Eq. (1)] converges reasonably rapidly, the energy $E(\sigma)$ of *any configuration* can be obtained almost immediately by simply calculating the spin products and summing Eq. (1). Because the Ising representation of the energy can be calculated rapidly, and is also a linear function of the spin products, one can readily use Eq. (1) and (i) apply linear programming techniques³ to find ground state structures, (ii) use statistical-mechanics techniques (Monte Carlo⁴⁻⁶ and cluster variation methods⁷) to calculate phase diagrams,⁸⁻¹⁰ (iii)

calculate excess enthalpies^{8,11} and free energies^{8,11} at $T \neq 0$, (iv) calculate the energy of an arbitrarily complex configuration such as superlattice¹² and antiphase boundaries,¹³ and (v) calculate short-range^{14,15} and long-range^{16,17} order parameters.

The problem with representation (1) is that often atoms move off their ideal lattice sites (“relaxation”) and that when this happens the convergence of Eq. (1) becomes slow.¹⁸⁻²⁰ Relaxation takes the form¹ of “volume deformation” (compression and dilation of pure solid A and B to the equilibrium volume of configuration σ) as well as the displacement of the unit cell vectors (“cell external relaxations”) and symmetry-allowed atomic displacements within the unit cell (“cell-internal relaxations”). The degree of relaxation scales²⁰ with the relative A -to- B lattice size mismatch, the average bulk modulus, and inversely with the average phonon frequency squared. Relaxation in alloys has been observed by extended x-ray-absorption fine structure (EXAFS) both in metallic²¹ and in semiconducting^{22,23} systems. Most of the standard theories of calculating the interaction energies J neglect, however, all forms of relaxation. This is true for the “direct configurational averaging (DCA) method,”^{24,25} the “generalized perturbation method”²⁶ (GPM), the “concentration-wave (CW) method,”^{27,28} and the “embedded cluster method”²⁹ (ECM). Recent calculations have demonstrated, however, the importance of incorporating relaxation effects into Eq. (1): These can alter the interaction energies of transition-metal alloys by as much as 200%,²⁰ change the predicted symmetry of the ground-state structure in NiPt,^{30,31} narrow significantly the single-phase domains in the Cu-Au phase diagram,³² lower the miscibility gap temperature of semiconductor alloys by a few hundred degrees,^{1,8,11,12} change the sign of the ordering energy of NiAu,³⁰ and shift peaks in the density of states of Cu-Au (Ref. 33) and Cu-Pd (Ref.

33) by as much as ~ 1 eV. Also, while standard elasticity theory^{12,18,34} predicts that long-period superlattices A_nB_n have an *orientation-dependent* energy, this feature cannot be captured in any finite real-space cluster expansions that neglects relaxation.

A number of efforts have recently been made to introduce phenomenologically relaxation into the calculation of the interaction energies^{35–39} J . None of these, however, includes cell internal and cell external relaxation nor do they solve the above mentioned problem of long-period superlattices.

We have recently developed an efficient scheme for including all form of relaxation in Eq. (1). The method combines the direct inversion method (Connolly-Williams⁴⁰) with Khachatryan’s concentration wave method.⁴¹ The result is an Ising-type Hamiltonian using a both real-space and reciprocal-space interaction energies. All of the interaction energies are derived from first-principles local-density-approximation⁴² (LDA) calculations for a small ($\lesssim 20$) set of structures. The interaction energies include the full effects of atomic relaxations, which allows us to make predictions for the energies of very large structures (with thousands of atoms) in which all of the atoms are fully relaxed. Since we derive interaction energies $\{J\}$ that directly incorporate relaxation effects on the *energy*, we can use Eq. (1) to predict the relaxed $E(\sigma)$ of any substitutional configuration without having to determine the actual relaxed atomic *positions*.

In this work we apply the method both to a semiconductor system GaP-InP and to a transition-metal system Cu-Pd, using the LDA to construct Eq. (1) and the Monte Carlo^{4–6} (MC) and simulated-annealing⁴³ methods to perform ground-state searches for large unit cells and to solve for thermodynamic quantities. We also predict the degree of short-range order (SRO) in a simple and natural way, since our reciprocal-space energy expression is a function of the diffuse scattering intensity, which is the Fourier transform of the Cowley SRO parameters.^{44,45}

The paper is organized as follows: We present in Sec. II a brief summary of the mixed real- and reciprocal-space expression for the total energy. The interaction energies used in the total-energy expression are derived from LDA calculations for a small set of ordered structures. Section III describes the details of the LDA calculations, and how we extract the interaction energies from them. The total-energy expression contains a reciprocal-space part that is related to the diffuse scattering and to the SRO parameters. Section IV A describes the search of the ground-state structures, while in Sec. IV B we describe how this reciprocal-space energy can be efficiently implemented in a MC simulation and how to extract the SRO parameters from the simulation. Sec. V describes our implementation of simulated annealing and the results of ground-state searches for $\text{Ga}_{1-x}\text{In}_x\text{P}$ and $\text{Cu}_{1-x}\text{Pd}_x$ ground states, and the order-disorder transition temperatures. In Sec. VI we show our results for SRO in $\text{Cu}_{1-x}\text{Pd}_x$ and $\text{Ga}_{1-x}\text{In}_x\text{P}$ and compare this calculated SRO with the results of diffuse scattering experiments. Section VII describes how we use cluster expansion to study the stability of long-period superlattices

which is outside the range of the direct LDA calculations. Finally, Sec. VIII summarizes the results.

II. FORMULATING THE CLUSTER EXPANSION OF THE TOTAL ENERGY: SUMMARY OF RESULTS

Accurate first-principles total-energy calculations (e.g., using the LDA) can be conveniently performed only on a limited set (out of 2^N possibilities) of rather simple lattice configurations. For example, one can directly compute the total energy $E_{\text{direct}}(\sigma_s)$ of a few ordered, periodic configurations $\{\sigma_s\}$ with a reasonably small number of atoms in the unit cells. Focusing on the *relative* energies we define the formation energy of structure σ_s as

$$\Delta E_{\text{direct}}(\sigma_s) = E_{\text{direct}}(\sigma_s) - [(1-x)E(A, V_A) + xE(B, V_B)], \quad (2)$$

which is taken with respect to the energy of equivalent amounts of the constituent solids A and B at their respective equilibrium volumes V_A and V_B . Here $E_{\text{direct}}(\sigma_s)$ denotes the total energy of the directly calculated (i.e., no cluster expansion) *fully relaxed* configuration σ_s . Our task here is to use a set of such directly calculated first-principles formation energies of simple (s) configurations $\{\sigma_s\}$ to define a general cluster expansion of the type of Eq. (1) applicable to any configuration. To this end, the Ising series of Eq. (1) is first cast in terms of lattice-averaged functions. The lattice is broken into a set of “figures” f each being a specific set of sites, such as a nearest-neighbor pair or a nearest-neighbor triangle. Since the interaction energies have the full symmetry of the lattice, we can average the spin products of Eq. (1) over each class F of symmetry-equivalent “figures.” This defines a lattice-average spin product for F ,

$$\bar{\Pi}_F(\sigma) = \frac{1}{ND_F} \sum_f \hat{S}_{i_1}(\sigma) \hat{S}_{i_2}(\sigma) \cdots \hat{S}_{i_m}(\sigma), \quad (3)$$

where f run over the ND_F figures in class F , and the spin indices run over the m sites of figure f . In the remainder of this paper, we will use the term figure for a class of equivalent figures, as in “the nearest-neighbor pair figure.” The set $\{\bar{\Pi}_F(\sigma)\}$ defines² a complete, orthogonal set of basis functions over the space defined by $\{\sigma\}$. This means that we can rigorously expand any lattice property $\mathcal{P}(\sigma)$ in terms of an appropriate set of J_F ’s (which need not be energies). In particular, we can also expand the energies of the configurations after all of the atoms have been fully relaxed—even though the atoms are no longer on their original lattice sites. We can therefore rewrite Eq. (1) as a cluster expansion (CE):

$$\Delta E_{\text{CE}}(\sigma) = N \sum_F D_F J_F \bar{\Pi}_F(\sigma). \quad (4)$$

We now take a few steps in anticipation of a possible slow convergence of Eq. (4):

First, rather than expand $\Delta E_{\text{direct}}(\sigma)$, we will expand the energy with respect to a reference (ref) energy,

$$\Delta E'_{\text{CE}}(\sigma) = \Delta E_{\text{direct}}(\sigma) - E_{\text{ref}}(\sigma). \quad (5)$$

Second, we will separate the sum in Eq. (4) into (i) a term including all pair interactions, which will be conveniently summed to infinity using the reciprocal-space concentration-wave formalism, and (ii) the many-body terms which will be cast in real space. This gives

$$\Delta E'_{\text{CE}}(\sigma) = N \sum_{\mathbf{k}} J(\mathbf{k}) |S(\mathbf{k}, \sigma)|^2 + N \sum_F D_F J_F \bar{\Pi}_F(\sigma), \quad (6)$$

where the first term includes *all* pair interactions and the second term extends to $F = \text{many-body figures}$. The Fourier transform of the real-space pair interaction $J_{0,n}$ between site 0 and site n is

$$J(\mathbf{k}) = \frac{1}{2} \sum_n^N J_{0,n} e^{i\mathbf{k} \cdot \mathbf{R}_n}, \quad (7)$$

while the Fourier transform of the spin variables is

$$S(\mathbf{k}, \sigma) = \frac{1}{N} \sum_l^N S_l(\sigma) e^{i\mathbf{k} \cdot \mathbf{R}_l}, \quad (8)$$

where \mathbf{R}_l (or \mathbf{R}_n) is the coordinate of the l th atomic site, and \mathbf{k} is a vector in the first Brillouin zone. For an ordered configuration σ , the $S(\mathbf{k}, \sigma)$ functions will only be nonzero for a finite set of points \mathbf{k} .

Assuming $E_{\text{ref}} = 0$ the mixed-space cluster expansion of Eq. (6) is entirely equivalent to the real-space form of Eq. (4). Laks *et al.*¹⁸ introduced, at this point, two modifications.

First, they required that $J(\mathbf{k})$ be a smooth function. This was accomplished by minimizing

$$M = \frac{1}{\alpha} \sum_{\mathbf{k}} J(\mathbf{k}) [-\nabla_{\mathbf{k}}^2]^{\lambda/2} J(\mathbf{k}), \quad (9)$$

where α is a normalization constant and the exponent λ is a parameter. *Second*, they selected E_{ref} of Eq. (5) to contain long-range interaction terms so that the expansion of $\Delta E_{\text{direct}}(\sigma) - E_{\text{ref}}(\sigma)$ converges faster than otherwise. If relaxation is unimportant, one might use $E_{\text{ref}} = 0$ just like in the Connolly-Williams⁴⁰ approach. However, when relaxation is significant, there is a singular $\mathbf{k} = 0$ term which can cause a slow decay of the real-space interactions, $J_{0,n}$ with distance $\mathbf{R}_0 - \mathbf{R}_n$. In this case one can choose¹⁸ $E_{\text{ref}}(\sigma)$ as the energy per atom of a $n \rightarrow \infty$ superlattice $A_n B_n$ whose layers are oriented along the direction $\hat{k}(\sigma)$ defined by the Lifshitz points of configuration σ [Eq. (8)]. This “constituents strain” (CS) energy ΔE_{CS} is the energy change when the bulk solids A and B are deformed from their equilibrium cubic lattice constants a_A and a_B to a common lattice constant a_{\perp} in the direction perpendicular to \hat{k} . For each direction \hat{k} , some equilibrium (eq) value of a_{\perp} will minimize this elastic energy. The composition-weighted energy of the

deformed constituents at this a_{\perp}^{eq} is

$$\Delta E_{\text{CS}}^{\text{eq}}(\hat{k}, x) = (1-x) \Delta E_A^{\text{epi}}(\hat{k}, a_{\perp}^{\text{eq}}) + x \Delta E_B^{\text{epi}}(\hat{k}, a_{\perp}^{\text{eq}}). \quad (10)$$

One can compute $\Delta E_{\text{CS}}^{\text{eq}}(\hat{k}, x)$ by performing LDA calculations for epitaxially constrained A and B solids along directions \hat{k} , finding a_{\perp}^{eq} at each \hat{k} . This “direct” calculation, however, has to be repeated for all directions $\hat{k}(\sigma)$ for which a given lattice configuration σ has $S(\mathbf{k}, \sigma) \neq 0$. Reference 18 has shown that this procedure can be simplified considerably if one assumes *harmonic* elasticity. In this case $a_{\perp}^{\text{eq}}(\hat{k})$ is computed analytically so the \hat{k} dependence of $\Delta E_{\text{CS}}^{\text{eq}}(\hat{k}, x)$ is given in closed form by

$$\begin{aligned} \frac{\Delta E_{\text{CS}}^{\text{eq}}(\hat{k}, x)}{4x(1-x)} &= \frac{1}{4} \frac{q_A(\hat{k}) q_B(\hat{k}) \Delta E_A(a_B) \Delta E_B(a_A)}{(1-x) q_A(\hat{k}) \Delta E_A(a_B) + x q_B(\hat{k}) \Delta E_B(a_A)}, \end{aligned} \quad (11)$$

where $\Delta E_A(a_B) = E_A(a_B) - E_A(a_A)$ and $\Delta E_B(a_A) = E_B(a_A) - E_B(a_B)$, and $E_A(a)$ and $E_B(a)$ are the energies of *bulk cubic* A and B at the lattice constant a . The function $q(\hat{k})$ is

$$q(\hat{k}) = \frac{\Delta E^{\text{epi}}(\hat{k}, a_{\perp})}{\Delta E(a)} = 1 - \frac{\alpha}{1 + \beta \gamma(\hat{k})}, \quad (12)$$

where α and β are determined from epitaxial LDA calculations of pure A and B at *just two to three directions* \hat{k} , and $\gamma(\hat{k})$ is a purely geometrical factor given by

$$\gamma(\hat{k}) = \gamma(\phi, \theta) = \sin^2(2\theta) + \sin^4(\theta) \sin^2(2\phi). \quad (13)$$

Thus, simple LDA calculations for epitaxially deformed A and B in two to three directions determined α and β . Along with two cubic bulk calculations of the energy $\Delta E_A(a_B)$ of pure A at the lattice constant of B and similarly for $\Delta E_B(a_A)$, these give the full composition and direction dependence of the long-period superlattice energy $\Delta E_{\text{CS}}^{\text{eq}}(\hat{k}, x)$ of Eq. (11). The reference energy $E_{\text{ref}}(\sigma)$ which we subtract from $\Delta E_{\text{direct}}(\sigma)$ before a cluster expansion is attempted is hence

$$E_{\text{ref}}(\sigma) = N \sum_{\mathbf{k}} J_{\text{CS}}(\mathbf{k}) |S(\mathbf{k}, \sigma)|^2, \quad (14)$$

where

$$J_{\text{CS}}(\mathbf{k}) = J_{\text{CS}}(\hat{k}, x) = \frac{\Delta E_{\text{CS}}^{\text{eq}}(\hat{k}, x)}{4x(1-x)}. \quad (15)$$

The reference energy of Eq. (14) corresponds to an infinite series of *real-space* elastic interactions. Removing them from the relaxed LDA-calculated energies $\Delta E_{\text{direct}}(\sigma)$ prior to a cluster expansion significantly accelerates the convergence of this expansion.¹⁸

Combining a set $\{\Delta E_{\text{direct}}(\sigma_s)\}$ of LDA calculations on simple configurations $\{\sigma_s\}$ with Eqs. (5)–(9) we then

solve

$$\sum_{\sigma_s}^{N_\sigma} \omega_{\sigma_s} |\Delta E_{\text{direct}}(\sigma_s) - E_{\text{ref}}(\sigma_s) - \Delta E'_{\text{CE}}(\sigma_s)|^2 + tM = \text{Min}, \quad (16)$$

where ω_{σ_s} are statistical weights for configuration σ_s , ΔE_{direct} is given by Eq. (2), the reference energy is given by Eqs. (14) and (15), the cluster expanded energy $\Delta E'_{\text{CE}}$ is given by Eq. (6), the smoothness condition M is from Eq. (9), and t is a Lagrange multiplier. The inputs to our calculation are N_σ LDA configurational energies $\{\Delta E_{\text{direct}}(\sigma)\}$, the LDA epitaxial parameters of Eq. (12), and the values of λ and t . The output consists of the pair spectrum $J(\mathbf{k})$ (or, equivalently, its Fourier transform $J_{0,n}$) and the many-body interactions $\{J_F\}$. Together these enable calculation of the excess energy of *any* of the 2^N configurations σ from

$$\Delta E_{\text{CE}}(\sigma) = \Delta E'_{\text{CE}}(\sigma) + E_{\text{ref}}(\sigma). \quad (17)$$

Convergence is tested by applying Eq. (17) to a set of structures $\{\sigma'\}$ not used in constructing the CE of Eq. (16). If the predictions errors

$$\delta(\sigma') = |\Delta E_{\text{CE}}(\sigma') - \Delta E_{\text{direct}}(\sigma')| \quad (18)$$

are larger than a prescribed tolerance, more many-body figures and input structures are added to the expansion (6). This method has been tested¹⁸ previously by comparing the prediction $\Delta E_{\text{CE}}(\sigma')$ to directly calculated energies of huge supercells (up to 1000 atoms) with different symmetries (abrupt and interdiffused superlattices, random alloys, impurities). The direct calculations as well as the corresponding CE were done using valence force field method.⁴⁶ Excellent agreement was found. Here we extend the method to first-principles local-density-approximation⁴² (LDA) approach.

III. EVALUATING THE CLUSTER EXPANSION FROM LOCAL-DENSITY TOTAL-ENERGY CALCULATIONS

A. LDA calculation of ΔE_{direct} for ordered structures

We calculate the total energies [Eq. (2)] of periodic crystals in the LDA. For the purpose of constructing *and* testing the CE, we have chosen ~ 30 ordered structures which have a small number of atoms per cell (≤ 16), so that we can accurately calculate their total energies in a reasonable amount of computer time. These structures^{33,47-49} are defined in Tables I and II. They

TABLE I. Directly calculated relaxed LDA excess energies ΔE_{direct} (error ± 2 meV/atom) and the corresponding cluster expanded [Eqs. (16) and (17)] formation energies ΔE_{CE} (in meV/atom) for GaP-InP. Many of the structures calculated here can be characterized as a $(\text{GaP})_p(\text{InP})_q$ superlattice in orientation \hat{G} . We use the conventional structure (or prototype) name when available, and assign our own label otherwise. The “special quasirandom structures” (SQS’s) are structures with small number of atoms/cell used to mimic the random alloy. The structural information for these SQS’s is given in Ref. 47. The structures labeled here with the asterisk are used in the fit of Eq. (16); others are for predictions.

Orientation formula	[001]	[011]	[012]	[111]	[113]
<i>AB</i>	<i>L1</i> ₀ *	<i>L1</i> ₀ *	<i>L1</i> ₀ *	<i>L1</i> ₁ *	<i>L1</i> ₁ *
ΔE_{direct}	22.6	22.6	22.6	36.1	36.1
ΔE_{CE}	22.6	22.6	22.6	36.1	36.1
<i>A</i> ₂ <i>B</i>	β 1	MoPt ₂	MoPt ₂	α 1	MoPt ₂
ΔE_{direct}	19.8	11.4	11.4	31.7	11.4
ΔE_{CE}	17.0	11.6	11.6	29.1	11.6
<i>AB</i> ₂	β 2	MoPt ₂	MoPt ₂	α 2	MoPt ₂
ΔE_{direct}	20.5	11.7	11.7	32.0	11.7
ΔE_{CE}	17.6	8.8	8.8	30.2	8.8
<i>A</i> ₃ <i>B</i>	<i>Z</i> 1	<i>Y</i> 1	<i>DO</i> ₂₂	<i>V</i> 1	<i>W</i> 1*
ΔE_{direct}	16.9	13.7	11.3	26.3	17.4
ΔE_{CE}	16.6	14.1	11.8	26.1	17.4
<i>AB</i> ₃	<i>Z</i> 3	<i>Y</i> 3	<i>DO</i> ₂₂	<i>V</i> 3	<i>W</i> 3*
ΔE_{direct}	18.2	13.6	8.0	27.6	15.7
ΔE_{CE}	17.4	12.4	7.0	27.4	15.8
<i>A</i> ₂ <i>B</i> ₂	<i>Z</i> 2*	<i>Y</i> 2*	“40”*	<i>V</i> 2*	<i>W</i> 2
ΔE_{direct}	22.7	15.2	7.5	35.5	15.3
ΔE_{CE}	22.7	15.2	7.5	35.5	15.1
	other structures				
	<i>A</i> *	<i>B</i> *	<i>L</i> ₁₂ * (<i>A</i> ₃ <i>B</i>)	<i>L</i> ₁₂ * (<i>AB</i> ₃)	
ΔE_{direct}	0.0	0.0	19.5	14.4	
ΔE_{CE}	0.0	0.0	19.5	14.3	
	SQS8A (<i>A</i> ₄ <i>B</i> ₄)		SQS8B (<i>A</i> ₄ <i>B</i> ₄)		
ΔE_{direct}	16.6		16.3		
ΔE_{CE}	17.5		19.0		

correspond to short-period superlattices in a range of compositions and orientations. For Cu-Pd, the L_{12} -based long-period superstructures (LPS's) are also included (see Fig. 1). The LDA equations are solved self-consistently by the linearized augmented-plane-wave (LAPW) method.⁵⁰ For Cu-Pd we used the Wigner⁵¹ exchange-correlation potential, while for GaP-InP we used the Ceperley-Alder exchange-correlation potential as parametrized by Perdew and Zunger.^{52,53} The core states are treated fully relativistically, while the valence states are treated semirelativistically (without spin-orbit interaction). No shape approximation is made for either the potential or the charge density. Inside the muffin-tin spheres, the nonspherical charge density and potential are expanded in terms of lattice harmonics of angular momentum $l \leq 8$. A basis set of about ~ 90 LAPW's/atom are used (equivalent to kinetic energy cutoff of 16.7 Ry). The Brillouin zone integration is performed using the spe-

cial \mathbf{k} -point methods.⁵⁴ About 60–400 special \mathbf{k} points in the irreducible Brillouin zone (BZ) (depending on the structure and the material) are used for the metallic compounds; for GaP-InP ten special \mathbf{k} points for the zinc-blende structure and their symmetry-equivalent \mathbf{k} points for the other superstructures are used. We have used relaxed atomic positions, i.e., allow the cell external lattice parameters and the position of the atoms inside the unit cell (that are not fixed by symmetry) to vary so as to minimize $\Delta E(\sigma, V_\sigma)$. For Cu-Pd we assume $V_\sigma = (1-x)V_A + xV_B$. When structural degrees of freedom are forbidden by symmetry (e.g., in L_{12}), relaxation does not exist; otherwise, it lowers the energy. Table III shows that this lowering can be significant in structures possessing a number of such structural degrees of freedom (e.g., $\beta 1, \beta 2, Z 2$), but is small in more symmetrical structures (e.g., DO_{22} , "40"). The convergence error for the total energy is estimated to be about 10 meV/atom for

TABLE II. Directly calculated relaxed LDA excess energies $\Delta E_{\text{direct}}(\sigma)$ (error ± 10 meV/atom) and the corresponding cluster expanded [Eqs. (16) and (17)] formation energies $\Delta E_{\text{CE}}(\sigma)$ (in meV/atom) for Cu-Pd. Many structures calculated here can be characterized as a Cu_pPd_q superlattice in orientation \hat{G} . We use the conventional structure (or prototype) name when available and assign our own label otherwise. The definition of the $D1$, $D7$, and $D4$ structures is given in Ref. 9. The "special quasirandom structures" (SQS's) are structures with small number of atoms/cell used to mimic the random alloy. The structural information for these SQS's is given in Refs. 47 and 33. The L_{12} -based one-dimensional long-period superlattices (LPS's) are denoted by their Fisher-Selke (see Ref. 48 and Fig. 1) notation which specifies, between angular brackets, the sequence of nonantiphased domains. The structures labeled here with the asterisk are used in the fit of Eq. (16); others are for predictions.

Orientation formula	[001]	[011]	[012]	[111]
AB	$L1_0^*$	$L1_0^*$	$L1_0^*$	$L1_1^*$
ΔE_{direct}	-86.3	-86.3	-86.3	-82.0
ΔE_{CE}	-82.2	-82.2	-82.2	-81.0
A_2B	$\beta 1^*$	MoPt ₂	MoPt ₂	$\alpha 1^*$
ΔE_{direct}	-45.6	-80.0	-80.0	-40.3
ΔE_{CE}	-46.3	-74.6	-74.6	-39.3
AB_2	$\beta 2$	MoPt ₂	MoPt ₂	$\alpha 2^*$
ΔE_{direct}	-72.0	-45.7	-45.7	-49.2
ΔE_{CE}	-65.6	-54.6	-54.6	-49.8
A_3B	$Z1^*$	Y1	DO_{22}^*	V1*
ΔE_{direct}	-32.9	-65.9	-76.4	-20.0
ΔE_{CE}	-41.0	-56.4	-77.8	-22.2
AB_3	$Z3^*$	Y3	DO_{22}^*	V3
ΔE_{direct}	-50.2	-36.6	-46.4	-34.1
ΔE_{CE}	-59.2	-47.5	-47.0	-34.4
A_2B_2	$Z2^*$	Y2	"40"*	V2
ΔE_{direct}	-72.0	-63.2	-84.6	-29.5
ΔE_{CE}	-62.7	-67.7	-83.8	-18.8
	other structures			
	A*	B*	$L_{12}(A_3B)^*$	$L_{12}(AB_3)^*$
ΔE_{direct}	0.0	0.0	-85.0	-53.4
ΔE_{CE}	2.5	2.1	-85.9	-53.0
	$D1(A_7B)$	$D7(AB_7)$	$D4(A_4B_4)$	
ΔE_{direct}	-38.1	-31.8	-65.3	
ΔE_{CE}	-30.7	-24.9	-65.5	
	SQS8A (A_4B_4)	SQS8B (A_4B_4)	SQS14 (A_6B_2)	
ΔE_{direct}	-57.1	-67.8	-48.6	
ΔE_{CE}	-54.5	-69.7	-43.6	
	$DO_{23}(A_6B_2)$	LPS $\langle 21 \rangle (A_9B_3)$	LPS $\langle 3 \rangle (A_9B_3)^*$	LPS $\langle 4 \rangle (A_{12}B_4)$
ΔE_{direct}	-83.9	-80.7	-90.0	-87.4
ΔE_{CE}	-85.8	-82.4	-88.0	-88.1

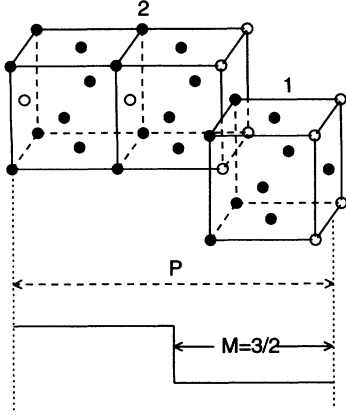


FIG. 1. A long-period superstructure can be constructed from an $L1_2$ unit by modulating it with a square wave. An antiphase boundary is introduced whenever the modulation function changes sign and the structure is denoted by specifying the length of nonantiphased domains in the unit cell. Here we show the LPS $\langle 21 \rangle$ (using the Fished and Selke notation in Ref. 48), which has modulation wavelength $M = \frac{3}{2}$ (in units of the fcc lattice parameter), and fundamental reciprocal-space wave vector $\mathbf{k} = \langle 1 \frac{1}{2M} 0 \rangle \equiv \langle 1 \frac{1}{3} 0 \rangle$. See Ref. 49 for a more detailed descriptions of these LPS's.

Cu-Pd and about 2 meV/atom for the GaP-InP system. We will see later (Sec. III B) that the cluster expansion fitting errors are equal or *lower* than these LAPW errors. For configurations with a large number of structural degrees of freedom, we calculate quantum-mechanical atomic force⁵⁵ to aid the total-energy minimization process.

Tables I and II give the calculated $\Delta E_{\text{direct}}(\sigma)$ for $(\text{GaP})_n(\text{InP})_m$ and $(\text{Cu})_n(\text{Pd})_m$ structures, respectively. The LDA results for GaP-InP shown here are slightly different from those given in Ref. 8, reflecting a better convergence in the present calculation. Figure 2 shows the LAPW-calculated $\Delta E_{\text{direct}}(\sigma)$ for (a) $\text{Ga}_{1-x}\text{In}_x\text{P}$ and (b) $\text{Cu}_{1-x}\text{Pd}_x$ in a number of crystal structures and compositions. While these two systems have a similar lattice constant mismatches (7.4% for GaP-InP and 7.3% for Cu-Pd) and form fcc-based solid solutions at high temperatures, they exhibit drastically different alloying behaviors at low temperatures: The $\text{Ga}_{1-x}\text{In}_x\text{P}$ phase separates⁵⁶ into its constituents GaP and InP, while $\text{Cu}_{1-x}\text{Pd}_x$ form ordered compounds⁵⁷ (bcc-based CsCl structure at $x \sim 0.5$ and fcc-based $L1_2$ structure

at $x \sim 0.25$). These phase-separation (in $\text{Ga}_{1-x}\text{In}_x\text{P}$) and ordering (in $\text{Cu}_{1-x}\text{Pd}_x$) behaviors are already suggested by the signs of their $\Delta E_{\text{direct}}(\sigma)$ in Fig. 2: For all the calculated structures $\Delta E_{\text{direct}}(\sigma)$ are positive for $\text{Ga}_{1-x}\text{In}_x\text{P}$ and negative for $\text{Cu}_{1-x}\text{Pd}_x$. The dashed lines in Fig. 2 connect the lowest energies of the structures of Tables I and II. The maximum $\Delta E_{\text{direct}}(\sigma)$ among the calculated set is $\sim +40$ meV/atom for $\text{Ga}_{1-x}\text{In}_x\text{P}$; the minimum for $\text{Cu}_{1-x}\text{Pd}_x$ among the calculated set is ~ -90 meV/atom.

B. Cluster expanding $\Delta E(\sigma)$

The reference energy of Eqs. (14) and (15) is computed from the harmonic elasticity [Eqs. (11)–(13)]. This requires fitting LDA calculations of $\Delta E^{\text{epi}}(\hat{k}, a_{\perp})$ to Eq. (12). The fitting parameters α and β are given in Table IV. Figure 3 compares the constituent strain energy $\Delta E_{\text{CS}}^{\text{eq}}(\hat{k}, x)$ in GaP-InP and Cu-Pd as predicted by the harmonic elasticity theory of Eqs. (11)–(13) with $\Delta E_{\text{CS}}^{\text{eq}}(\hat{k}, x)$ as calculated directly by the LDA [Eq. (10)] in the three principal directions [001], [011], and [111]. The two results agree within 1 meV/atom for GaP-InP and 5 meV/atom for Cu-Pd.

We next proceed to cluster expand $\Delta E_{\text{direct}}(\sigma) - E_{\text{ref}}(\sigma)$ of Eq. (5). We thus need to choose (i) the configurations $\{\sigma_s\}$ used to construct the CE and (ii) the many-body figures $\{F\}$ used in the expansion.

(i) *Configurations*: For $\text{Ga}_{1-x}\text{In}_x\text{P}$, we used an input set of 12 structures denoted in Table I by asterisks, i.e., A, B, $L1_0$, $L1_2$, $L1_2$, “40”, $L1_1$, Z2, V2, Y2, W1, and W3 (this set has been denoted as “set s_2 ” in Ref. 18). We find that the interactions in Cu-Pd are longer ranged than in GaP-InP (see later); therefore more input structures are needed. We used an input set which includes 18 structures for $\text{Cu}_{1-x}\text{Pd}_x$, i.e., A, B, $L1_0$, $L1_2$, $L1_2$, “40”, $L1_1$, Z2, DO_{22} , DO_{22} , Z1, Z3, $\alpha 1$, $\alpha 2$, $\beta 1$, V1, D4, and LPS $\langle 3 \rangle$. These structures are denoted by asterisks in Table II. We use $\omega_{\sigma} = 1$ in Eq. (16).

(ii) *Figures*: The many-body figures considered are given in Table V. In addition to the nearest-neighbor three- (J_3) and four-body (J_4) interactions, we also included the following three- and four-body terms: K_3 , L_3 , M_3 , K_4 , and L_4 for Cu-Pd.

Having computed E_{ref} and selected configurations and figures, Eq. (16) is solved via a least squares fit. The results are used to predict via Eq. (17) the energies of

TABLE III. This table illustrates the importance of the lattice relaxation for structures having a number of internal degrees of freedom ($\beta 1$, Z2, $\beta 2$) and relative unimportance of relaxation for more symmetrical structures (DO_{22} , “40”). The structures are defined in Table II. Energies are in meV/atom.

	$\beta 1$ (Cu_2Pd)	Z2 (Cu_2Pd_2)	$\beta 2$ (CuPd_2)
$\Delta E_{\text{unrelaxed}}$	-36.4	-4.3	-48.6
$\Delta E_{\text{relaxed}}$	-45.6	-72.0	-72.0
	DO_{22} (Cu_3Pd)	“40” (Cu_2Pd_2)	DO_{22} (CuPd_3)
$\Delta E_{\text{unrelaxed}}$	-75.5	-76.4	-46.4
$\Delta E_{\text{relaxed}}$	-76.4	-84.6	-46.4

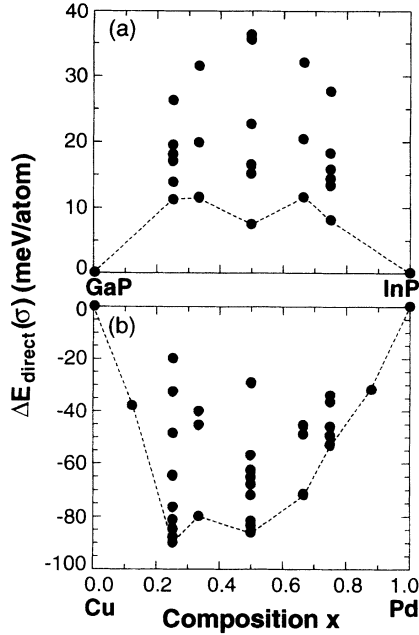


FIG. 2. Directly calculated LAPW excess energies [Eq. (2)] $\Delta E_{\text{direct}}(\sigma)$ for (a) $\text{Ga}_{1-x}\text{In}_x\text{P}$ and (b) $\text{Cu}_{1-x}\text{Pd}_x$. The dashed lines connect the lowest energy at each composition among the calculated set.

other structures. Figure 4 illustrates the prediction and fitting error [average of $\delta(\sigma')$ in Eq. (18)] as a function of the number of pair interactions (while the other fitting parameters are kept fixed at their optimal values). The dash-dotted lines denote the errors among the structures used in the fit (structures denoted with asterisks in Tables I and II). The dashed lines denote the average prediction errors for structures *not* used in the fit, while the solid lines denote the maximum prediction error in either sets. It is quite apparent from Fig. 4 that $\text{Ga}_{1-x}\text{In}_x\text{P}$ has a much shorter interaction range (requiring ~ 30 pair figures) than $\text{Cu}_{1-x}\text{Pd}_x$ (requiring ~ 190 pair figures). In our previous work on the Cu-Pd alloy,⁹ a much shorter range of interaction (up to fourth nearest neighbor) was used. Tables I and II compare the energies $\Delta E_{\text{CE}}(\sigma)$ obtained in the cluster expansion with the directly calculated values $\Delta E_{\text{direct}}(\sigma)$: For GaP-InP, where a typical excess energy $\Delta E(\frac{1}{2})$ is around +20 meV/atom, we find a fitting error of 0.01 meV/atom and an average prediction error for the 17 structures *not* used in the fit of 1.66 meV/atom. For Cu-Pd where a typical excess energy $\Delta E(\frac{1}{2})$ is around -70 meV/atom we find an average fitting error of 3.9 meV/atom, an average prediction error

TABLE IV. The dimensionless fitting parameters α and β for $E_{\text{ref}} = \Delta E_{\text{CS}}^{\text{eq}}(\hat{k}, x)$ of Eqs. (11) and (12). The energy $\Delta E_A(a_B)$ of cubic A at the equilibrium constant of B is in units of meV/atom.

	$\Delta E_A(a_B)$	α	β
GaP	240.5	0.6131	0.3570
InP	360.0	0.7644	0.1317
Cu	326.3	0.8656	0.4015
Pd	866.0	0.8064	0.1133

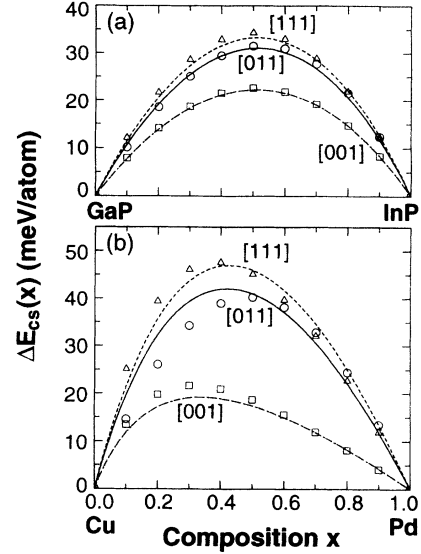


FIG. 3. Comparison of the elastic energy $\Delta E_{\text{CS}}^{\text{eq}}(\hat{k}, x)$ predicted by harmonic elasticity [Eqs. (11)–(13)] with those calculated directly by the LDA for (a) GaP-InP and (b) Cu-Pd. The LDA results for the [00], [011], and [111] directions are indicated by squares, circles, and triangles, respectively. The harmonic elastic theory predictions for these three direction are indicated by dash-dotted, solid, and dashed lines, respectively.

of 6.2 meV/atom (for 16 structures that are not used in the fit). Recall (Sec. III) that the inherent LAPW convergence errors are 10 meV/atom and 2 meV/atom for Cu-Pd and GaP-InP, respectively. Thus, these errors are the real limiting factors at this time: It makes no sense to improve the CE before the LAPW errors are reduced. Within these error limits, it is now possible to predict from Eq. (17) the relaxed LDA energies of complex many-atom structures essentially effortlessly. Note that the CE error $\delta(\sigma)$ is a non-negligible part of ΔE for *nonreactive* systems (small ΔE 's, e.g., Cu-Pd or GaP-InP) but the situation is much better in *reactive* alloys having large ΔE 's (e.g., Ni-Al with $\Delta E \sim -600$ meV/atom or Pt-Ti with $\Delta E \sim -900$ meV/atom).

Figure 5 shows the pair interaction energies $J(\mathbf{k})$ of Eq. (7) in the first Brillouin zone, while Fig. 6 shows the Fourier transform, i.e., real-space pair interaction energies $J_{0,n}$ of Eq. (7). Note that while for $\text{Ga}_{1-x}\text{In}_x\text{P}$ the pair energies $J_{0,n}$ have both positive and negative parts, for $\text{Cu}_{1-x}\text{Pd}_x$ they are mostly “antiferromagnetic” [positive $J_{0,n}$], with only a few of them slightly negative. We see that the minima of $J(\mathbf{k})$ occur at the W ($\mathbf{k} = \langle 1\frac{1}{2}0 \rangle$) point for GaP-InP and between the W and X points for Cu-Pd; we will see later in Secs. VIB and VIC that these \mathbf{k} points correspond to the peaks in the calculated diffuse scattering intensity due to short-range order at high temperatures for these materials.

IV. APPLICATIONS OF THE CLUSTER EXPANSION

This section describes how our mixed-basis cluster expansion

TABLE V. The vertices of multibody interactions of the fcc structure used here (in unit of $\frac{a}{2}$, where a is the lattice parameter.) The multibody interactions (including the degeneracy factor D_F) are given (in meV/atom) for GaP-InP and Cu-Pd.

Cluster type	Designation	Vertices	GaP-InP	Cu-Pd
Null	J_0		-9.29	-100.41
Point	J_1	(0,0,0)	-2.97	14.66
Triplets	J_3	(0,0,0) (1,1,0) (1,0,1)	2.96	-26.87
	K_3	(0,0,0) (1,1,0) (2,0,0)		8.37
	L_3	(0,0,0) (1,1,0) (2,1,1)		6.16
	M_3	(0,0,0) (1,1,0) (0,0,2)		-2.50
Quadruplets	J_4	(0,0,0) (1,1,0) (1,0,1) (0,1,1)	0.02	6.26
	K_4	(0,0,0) (1,1,0) (1,0,1) (2,0,0)		-13.70
	L_4	(0,0,0) (1,1,0) (1,0,1) (2,1,1)		-1.48

$$\Delta E_{CE} = N \sum_{\mathbf{k}} [J(\mathbf{k}) + J_{CS}(\mathbf{k})] |S(\mathbf{k}, \sigma)|^2 + N \sum_F D_F J_F \bar{\Pi}_F(\sigma) \quad (19)$$

can be used with the Monte Carlo simulated-annealing method to perform (a) ground-state searches of the stablest, $T = 0$ configurations, (b) calculation of the $T \neq 0$ short-range order, and (c) calculations of composition-temperature phase diagram.

A. Ground-state search

Finding the ground-state for a Hamiltonian of the type of Eq. (1) is a classical problem in magnetism and in

the theory of alloys.⁵⁸ The ground-state problem can be solved using the linear programming method.²⁵ For fcc alloys, the most complete search for the ground state was given by Kanamori and Takehashi;^{3,59} for bcc, it was given by Finel and Ducastelle.⁶⁰

We first should define what we understand by the ground state of the alloy. Let σ , α , and β be three configurations with concentration of B atoms $x(\sigma)$, $x(\alpha)$, and $x(\beta)$ in the order $x(\alpha) \leq x(\sigma) \leq x(\beta)$. If $E(\sigma)$ is larger than the linear average of $E(\alpha)$ and $E(\beta)$, that is, if

$$E(\sigma) > \frac{x(\sigma) - x(\beta)}{x(\alpha) - x(\beta)} E(\alpha) + \frac{x(\sigma) - x(\alpha)}{x(\beta) - x(\alpha)} E(\beta), \quad (20)$$

then configuration σ does not belong to the ground state because a mixture of the phases α and β would have a lower energy.

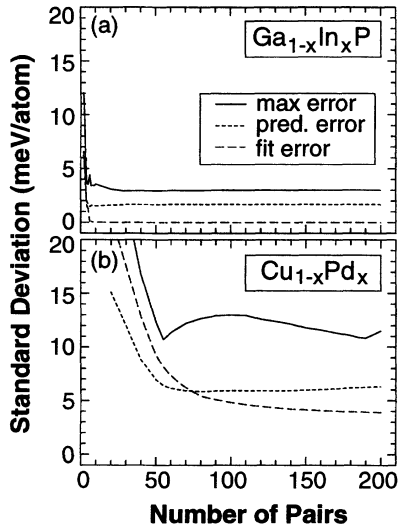


FIG. 4. This figure illustrates the prediction and fitting errors [average $\delta(\sigma)$ in Eq. (18)] as a function of number of pair interactions (the other fitting parameters are kept fixed at their optimal values) for (a) $\text{Ga}_{1-x}\text{In}_x\text{P}$ and (b) $\text{Cu}_{1-x}\text{Pd}_x$. The dash-dotted lines denote the fitting errors among the structures used in the fit (numbers with asterisks in Tables I and II). The dashed lines denote the average prediction errors for structures *not* used in the fit, while the solid lines denote the maximum prediction errors in either sets. Note that Cu-Pd requires considerably longer-range interactions than GaP-InP.

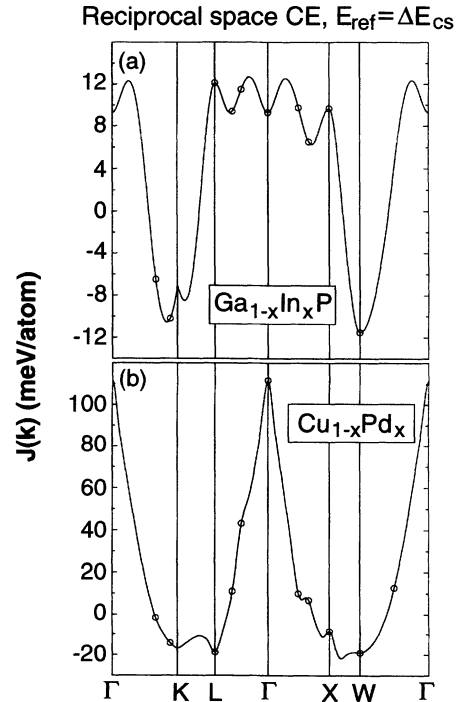


FIG. 5. Fourier transformation of the pair interaction energies $J(\mathbf{k})$ of Eq. (7) along the principal directions in the fcc Brillouin zone for (a) $\text{Ga}_{1-x}\text{In}_x\text{P}$ and (b) $\text{Cu}_{1-x}\text{Pd}_x$ using the mixed-basis cluster expansion.

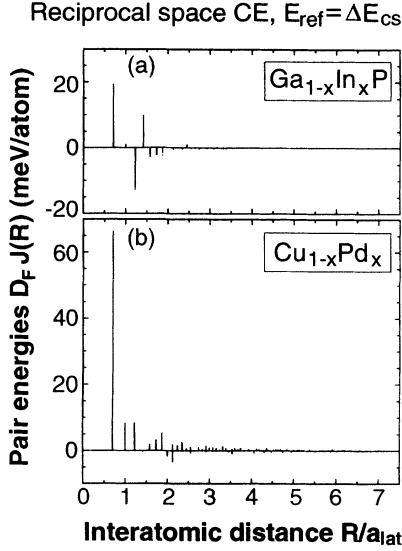


FIG. 6. Real-space pair interaction energies $J_{0,n}$ of Eq. (7) from the mixed-basis cluster expansion for (a) $\text{Ga}_{1-x}\text{In}_x\text{P}$ and (b) $\text{Cu}_{1-x}\text{Pd}_x$. Note that for $\text{Ga}_{1-x}\text{In}_x\text{P}$, $J_{0,n}$ is both positive and negative; $\text{Cu}_{1-x}\text{Pd}_x$ shows almost exclusive “antiferromagnetic” behavior (positive $J_{0,n}$).

While performing a ground-state search using linear programming is relatively easy, it has one major drawback: The lattice-averaged products $\bar{\Pi}_F$ functions of the ground state found may not correspond to those of an actual lattice structure. This is because the $\bar{\Pi}_F$ functions [Eq. (3)] of a real structure are constrained. The general constraint equations for the lattice products $\bar{\Pi}_F(\sigma)$ are unknown, and therefore cannot be included in the ground-state search. A related problem with using linear programming for ground-state searches is that the ground state found is identified only by its lattice products $\bar{\Pi}_F(\sigma)$; even if the ground state corresponds to a real structure, the only way to identify that structure really is by a trial-and-error search of lattice structures, until one is fortunate enough to find a real structure whose $\bar{\Pi}_F(\sigma)$ exactly match those of the ground state. The cause of these problems is that linear programming works only with the $\bar{\Pi}_F(\sigma)$, and never with actual lattice structures. Simulated annealing (SA), by contrast, performs a ground-state search directly on real lattice

structures. This guarantees that the ground state found is always a real structure, and that the exact structure is also known. The limitation for SA search is that one constrain the search to a finite cell; only structures commensurate with the cell can be obtained exactly.

B. Monte Carlo simulations and short-range order

In this section we describe how to implement the reciprocal-space cluster expansion in a Monte Carlo simulation and how to extract the SRO parameters from the results. Performing MC simulations for a reciprocal-space CE is a major challenge because the reciprocal-space energy is nonlocal in real space. This is because flipping one spin changes the $S(\mathbf{k})$ for *all* \mathbf{k} points. Since there are N \mathbf{k} points in an N -site lattice, updating $S(\mathbf{k})$ at each time step is an order- N process, compared to updating one or more $\bar{\Pi}_F$'s for a standard real-space Ising model (which is of order 1). This means that a MC simulation for a reciprocal-space CE is $O(N^2)$ as opposed to $O(N)$ for a real-space Ising model. (In this analysis we ignore possible changes in the convergence rate of the MC algorithm versus size.) One possible solution to this problem is to replace the spin flip move of the standard MC method—which is local in real space—with a move that changes $S(\mathbf{k})$ locally at a few points in reciprocal space. Such a scheme would again be $O(N)$. The problem with this idea is that there appears to be no way to define a local move that changes $S(\mathbf{k})$ at a few \mathbf{k} points but guarantees that when the new $S(\mathbf{k})$ is Fourier transformed to real space, it still corresponds to a set of spins that can be only ± 1 .

Instead we will retain the standard real-space MC spin flip with the following modification: We avoid the necessity of recalculating $S(\mathbf{k})$ for each move by directly calculating the change in $J(\mathbf{k})|S(\mathbf{k})|^2$ for each move. To do this we write $S(\mathbf{k})$ after l MC moves have been accepted as

$$S^{(l)}(\mathbf{k}) = S^{(0)}(\mathbf{k}) - \frac{2}{N} \sum_{i=1}^l \hat{S}(\mathbf{R}_i) e^{-i\mathbf{k}\cdot\mathbf{R}_i}, \quad (21)$$

where $S^{(0)}(\mathbf{k})$ is the initial value of $S(\mathbf{k})$ and $\hat{S}(\mathbf{R}_i)$ is the initial value of the spin that is flipped on move i . Since rejected moves do not change the spins, they make no contribution to subsequent moves. We now write the reciprocal-space energy after l accepted moves as

$$\begin{aligned} E_{\text{recip}}^{(l)} &= N \sum_{\mathbf{k}} J(\mathbf{k}) |S^{(l)}(\mathbf{k})|^2 \\ &= N \sum_{\mathbf{k}} J(\mathbf{k}) |S^{(l-1)}(\mathbf{k})|^2 + \frac{4}{N} \sum_{\mathbf{k}} J(\mathbf{k}) - 2\hat{S}(\mathbf{R}_l) \sum_{\mathbf{k}} J(\mathbf{k}) \left[S^{(l-1)}(\mathbf{k}) e^{-i\mathbf{k}\cdot\mathbf{R}_l} + \text{c.c.} \right] \\ &= E_{\text{recip}}^{(l-1)} + 2J(\mathbf{R}=\mathbf{0}) - 2\hat{S}(\mathbf{R}_l) \sum_{\mathbf{k}} J(\mathbf{k}) \left[S^{(0)}(\mathbf{k}) e^{-i\mathbf{k}\cdot\mathbf{R}_l} - \frac{2}{N} \sum_{i=1}^{l-1} \hat{S}(\mathbf{R}_i) e^{i\mathbf{k}\cdot(\mathbf{R}_i-\mathbf{R}_l)} + \text{c.c.} \right] \\ &= E_{\text{recip}}^{(l-1)} + 2J(\mathbf{R}=\mathbf{0}) - 2\hat{S}(\mathbf{R}_l) \sum_{\mathbf{k}} \left[J(\mathbf{k}) S^{(0)}(\mathbf{k}) e^{-i\mathbf{k}\cdot\mathbf{R}_l} + \text{c.c.} \right] \\ &\quad + \frac{4}{N} \hat{S}(\mathbf{R}_l) \sum_{i=1}^{l-1} \hat{S}(\mathbf{R}_i) \sum_{\mathbf{k}} \left[J(\mathbf{k}) e^{i\mathbf{k}\cdot(\mathbf{R}_i-\mathbf{R}_l)} + \text{c.c.} \right] \\ &= E_{\text{recip}}^{(l-1)} + 2J(\mathbf{R}=\mathbf{0}) - 4\hat{S}(\mathbf{R}_l) [S * J](\mathbf{R}_l) + 4\hat{S}(\mathbf{R}_l) \sum_{i=1}^{l-1} \hat{S}(\mathbf{R}_i) J(\mathbf{R}_l - \mathbf{R}_i), \end{aligned} \quad (22)$$

where c.c. stands for complex conjugate and $[S * J](\mathbf{R}) = \sum_{\mathbf{k}} J(\mathbf{k})S^{(0)}(\mathbf{k})e^{-i\mathbf{k}\cdot\mathbf{R}}$ is the convolution of $S^{(0)}(\mathbf{R})$ and $J(\mathbf{R})$, and we make use of the fact that both $J(\mathbf{R})$ and $[S * J](\mathbf{R})$ are real functions. This formula allows us to calculate the convolution once, using a fast Fourier transform (FFT), and then evaluate the change in reciprocal-space energy [first term of Eq. (6)] due to the l th spin flip using

$$\Delta E_{\text{recip}}^{(l)} = E_{\text{recip}}^{(l)} - E_{\text{recip}}^{(l-1)} = 2J(\mathbf{R} = \mathbf{0}) - 4\hat{S}(\mathbf{R}_l)[S * J](\mathbf{R}_l) + 4\hat{S}(\mathbf{R}_l) \sum_{i=1}^{l-1} \hat{S}(\mathbf{R}_i)J(\mathbf{R}_l - \mathbf{R}_i). \quad (23)$$

This equation requires the summation of $l + 1$ for each trial MC move, as opposed to N terms for a direct evaluation of the change in $S(\mathbf{k})$. When l grows too large, it will be faster to recalculate $[S * J](\mathbf{R})$ using an FFT routine, resetting $S^{(0)}(\mathbf{R}) \rightarrow S^{(l)}(\mathbf{R})$ and $l \rightarrow 0$. If we perform this procedure every m moves, the average cost of each move will be approximately

$$C_1 m/2 + C_2 N \ln(N)/m, \quad (24)$$

where the first term represents the cost of summing over Eq. (23) and the second the cost of performing two FFT's every m moves. This expression is minimized by $m = \sqrt{(2C_2/C_1)N \ln(N)}$. In our implementation we find that $m = \sqrt{N}$ is about the optimum choice. Using Eq. (23) improves the scaling of the algorithm from $N^2 \ln(N)$ to $N^{1.5} \sqrt{\ln(N)}$, and allows us to perform MC simulations on cells as large as 32^3 . In order to calculate the short-range-order (SRO) parameters, we first equilibrate the system using a small amount of moves per site (40) at the simulation temperatures; then we collect the SRO data over a longer Monte Carlo run (100 moves/per site). SRO is calculated using a $32 \times 32 \times 32$ ($16 \times 16 \times 16$) Monte Carlo simulation cell for Cu-Pd (GaP-InP).

C. Calculation of the phase diagram

We performed a standard Metropolis Monte Carlo simulation⁴ on the substitutional alloy system, using Eq. (23) to evaluate the energy change due to each Monte Carlo move. Since the reciprocal-space interaction energy $J(\mathbf{k})$ depends on the composition x through Eq. (11), our scheme requires that x remain fixed throughout a given simulation. To do this, we use a swap of sites as the basic Monte Carlo step: At each step, one A site and one B site are chosen at random, and the occupations of each site are reversed. Equation (23) is then used twice to account for the energy change due to two spin flips that constitute the move. The simulations are performed using periodic boundary conditions in all three dimensions.

Using the aforementioned MC simulated-annealing method, we can calculate the disorder-order transition temperature at different composition. We start the simulation at high temperatures for a random configuration, run the simulation for a prescribed number of Monte Carlo steps, and then lower the simulation temperature by multiplying it by a constant scale factor, typically 0.9. The annealing schedule is adjusted by hand, where both the number of steps at a given temperature and the scale factor can be adjusted for best performance. To determine the annealing schedule, we monitor the specific

heat (as calculated from the variance of the internal energy) at each simulation temperature. At temperatures where the specific heat is high, the annealing schedule is slowed down to allow for better equilibration. Note that simulated annealing tends to supercool a structure and therefore predicts lower transition temperatures than the standard Monte Carlo approach. In the standard Monte Carlo approach, at each temperature, one starts from the initial configuration (either random or ordered or a combination of the two), while in the simulated annealing one reuses the configuration from the higher temperature as the temperature is lowered; therefore one can use fewer steps at each temperature and zoom in on the ground state quickly in the SA approach.

The average value of $|S(\mathbf{k})|^2$ is calculated at each temperature, sampling its value at each step in which the full FFT is performed, and then weighting the value by the number of steps from the FFT until the next accepted step. This calculation adds a negligible amount to the calculation time. The value of $|S(\mathbf{k})|^2$ is directly proportional to the diffuse scattering intensity, and its Fourier transform gives the full set of Warren-Cowley SRO parameters (see Sec. VI). It also provides a convenient way to monitor the simulation for phase transitions, since these are accompanied by a large discontinuous jump in $|S(\mathbf{k})|^2$.

V. RESULTS: TRANSITION TEMPERATURES AND GROUND-STATE STRUCTURES

Using the simulated annealing technique, we have searched the coherent ground-state structures for $\text{Cu}_{1-x}\text{Pd}_x$ and $\text{Ga}_{1-x}\text{In}_x\text{P}$ and studied the temperature versus composition phase diagrams. Since this is a fairly costly procedure, we limited our search to only a few principal compositions, i.e., $x = \frac{1}{4}$, $\frac{1}{2}$, and $\frac{3}{4}$.

In Cu-Pd both coherent and incoherent ground states are ordered. The observed ground state⁵⁷ at $x = \frac{1}{4}$ is the $L1_2$ -based structure and at $x = \frac{1}{2}$ is the bcc-based CsCl structure denoted $B2$. Since our theory is based on the fcc lattice only, we will restrict our search to fcc-based structures only.

Table VI lists the predicted ground states along with the calculated transition temperature T_c^{MC} from the disordered phase to the order ground states. Figure 7 depicts the internal energies of the systems as a function of temperature. For $\text{Cu}_{0.75}\text{Pd}_{0.25}$, we find from cluster expansion that the $L1_2$ -based long-period superstructure LPS $\langle 4 \rangle$ structure (Fig. 1) is the ground state with its energy 0.1 meV/atom lower than LPS $\langle 3 \rangle$. Direct LAPW calculation, however, reverses the order, finding that LPS

TABLE VI. The table gives the ground-state fcc-based structures at $x = \frac{1}{4}$, $\frac{1}{2}$, and $\frac{3}{4}$, and their transition temperatures into disordered fcc alloy as obtained using Monte Carlo simulation (T_c^{MC}) and estimated using the ideal mixing entropy (IME) formula $kT_c^{\text{IME}}[x \ln x + (1-x) \ln(1-x)] = \delta E_{\text{ord}}$. We also give the cluster expanded energies $E_{\text{CE}}(\sigma)$ in meV/atom of the ground-state energy structures and the random alloys, as well as the ordering energies $\delta E_{\text{ord}}(\sigma) = \Delta E(\sigma) - \Delta E(\text{rand}, x)$.

	$x=0.25$	$x=0.50$	$x=0.75$
$\text{Cu}_{1-x}\text{Pd}_x$			
Structure	LPS (4)	Complex	Z3
$\Delta E_{\text{CE}}(\sigma)$	-88.1	-92.1	-59.2
$\Delta E_{\text{CE}}(\text{rand}, x)$	-41.8	-67.1	-44.0
δE_{ord}	-46.3	-25.0	-15.2
T_c^{MC} (K)	850	~ 300	~ 350
T_c^{IME} (K)	956	419	314
$\text{Ga}_{1-x}\text{In}_x\text{P}$			
Structure	Complex	Chalcopyrite	Complex
$\Delta E_{\text{CE}}(\sigma)$	9.1	7.5	6.0
$\Delta E_{\text{CE}}(\text{rand}, x)$	15.5	20.0	14.6
δE_{ord}	-6.4	-12.5	-8.6
T_c^{MC} (K)		~ 150	
T_c^{IME} (K)	133	209	177

$\langle 3 \rangle$ is lower in energy than LPS $\langle 4 \rangle$ by 2.6 meV/atom. We see from Fig. 7(b) that $\text{Cu}_{0.75}\text{Pd}_{0.25}$ undergoes a first-order phase transition from the high-temperature random alloy to the ordered LPS structure, with the transition temperatures of about 850 K. The observed Cu-Pd phase diagram⁵⁷ near $x = 0.25$ is quite complicated: One finds $L1_2$, and the $L1_2$ -based one-dimensional (1D) and 2D LPS's.^{49,61-63} The existence of LPS's, which is a mixture of the $L1_2$ and the DO_{22} structures, can be inferred from the small energy difference of only 8.6 meV/atom between the $L1_2$ and the DO_{22} structures (Table II). The assessed phase diagram⁵⁷ shows a transition from a disordered alloy to a 2D LPS at 730 K for $x = 0.25$, which is about 120 K below the presently calculated value.

Our results for $x = \frac{1}{2}$ cannot be compared with experiment since we restricted ourselves in this study to fcc superstructures (see, however, Refs. 9 and 10 where both fcc and bcc Cu-Pd was considered). At $x = \frac{1}{2}$, the lowest-energy fcc structure is rather complex and has a very low $T_c = 300$ K. The observed ground-state structure at $x = \frac{1}{2}$ is actually the bcc-based CsCl ($B2$) structure. The directly calculated LAPW value $\Delta H(B2) = -97.6$ meV/atom is indeed below the lowest calculated energy of fcc structures in agreement with experiment.

At $x = \frac{3}{4}$, the cluster expansion finds that the Z3 structure has the lowest energy: 6.2 meV/atom below the $L1_2$. However, direct LAPW calculation places the $L1_2$ below the Z3 by 3.2 meV/atom. The calculated transition temperature for Z3 is rather low: only ~ 350 K. This low ordering temperature probably explains why there is no ordered structure being observed at this composition.

Previously, Lu *et al.*^{9,10} calculated the ground states of Cu-Pd by extending the *real-space* CE (up to fourth nearest neighbor) to both fcc and bcc lattices. This enabled them to perform ground-state searches for the full composition range. They found the following ground states: $L1_2$ at $x = \frac{1}{4}$, $B2$ at $x = \frac{1}{2}$, $L1_2$ at $x = \frac{3}{4}$, and $D7$ at $x = \frac{7}{8}$.

In the case of GaP-InP, the *incoherent* ground state predicted by our theory corresponds to global phase separation, but the *coherent* ground state is ordered (Table VI) corresponding at $x = \frac{1}{2}$ to the chalcopyrite structure. The transition temperature from the disordered phase to this metastable chalcopyrite phase is about 150 K [Fig. 6(a)]. The lowest-energy structures for $x = \frac{1}{4}$ and

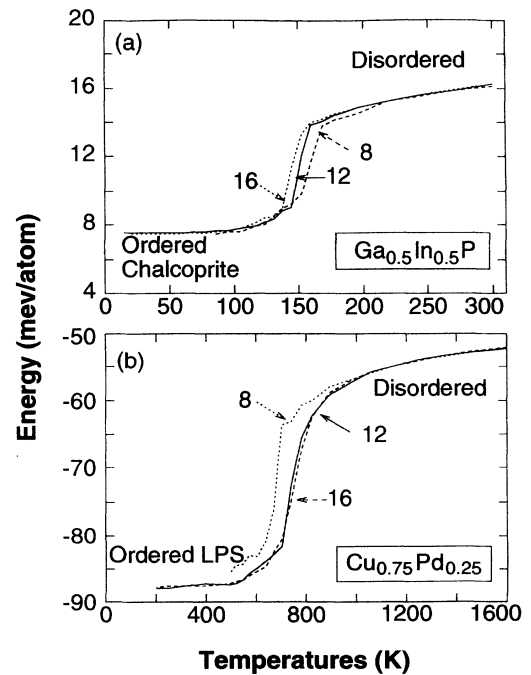


FIG. 7. The internal energies as a function of temperature for (a) $\text{Ga}_{0.5}\text{In}_{0.5}\text{P}$ and (b) $\text{Cu}_{0.75}\text{Pd}_{0.25}$. Here we show three different simulation cell sizes ($n \times n \times n$): dashed line, solid line, and dotted line are for $n = 8, 12,$ and 16 , respectively. The order-disorder transition temperatures are $T \sim 150$ K in (a) and $T \sim 620$ K in (b).

$\frac{3}{4}$ are identical having 16 fcc sites/cell (or 32 atoms/cell). It is rather difficult to estimate the transition temperatures for these compositions, since the internal energy versus temperature curves change rather gradual, unlike at $x = \frac{1}{2}$ where a clear first-order transition takes place.

Wei *et al.*⁸ have previously searched the coherent ground states of $\text{Ga}_{1-x}\text{In}_x\text{P}$ using an Ising interactions set which includes pairs up to fourth nearest neighbor and multiplets up to nearest-neighbor four-body interactions. At $x = \frac{1}{2}$, they found that chalcopyrite structure (a A_2B_2 [210] superlattice) is the lowest-energy structure, in agreement with the present result. Their calculated transition temperature (using the cluster variation

method rather than Monte Carlo simulated annealing and a shorter set of interactions) is 463 K, much higher than the present result. At $x = \frac{1}{4}$ and $\frac{3}{4}$, they found that the $C1$ and $C2$ structures (A_4BA_2B and B_4AB_2A [210] superlattice, with 8 fcc sites/cell) are the lowest-energy states, respectively. The pair $\bar{\Pi}_F$ of the $C1$ ($C2$) are identical to those of the presently found 16 fcc sites/cell structure up to the Ising interaction set used by Wei *et al.*⁸ The difference in pair $\bar{\Pi}_F$ with respect to our structure starts from the fifth pair.

Our cluster expansion can be used to compute the energy $\Delta E_{\text{CE}}(\text{random})$ of the ideally random alloy by taking a configuration average of Eq. (19). This gives

$$\Delta E_{\text{CE}}(\text{rand}, x) = [J_0 + J_1(2x - 1)] + (2x - 1)^2 \sum_n J_{0,n} + \sum_{k_F \geq 3} D_F J_F (2x - 1)^{k_F} + \int \Delta E_{\text{CS}}^{\text{eq}}(\hat{k}, x) d\hat{k} . \quad (25)$$

For the last term in Eq. (25), we use a slight approximation as we average $\Delta E_{\text{CS}}^{\text{eq}}(\hat{k}, x)$ over all solid angles (rather than averaging over the first Brillouin zone).¹⁸ Table VI gives the energy of a random alloy and also the “ordering energy” defined as the energy difference between an order structure and a random alloy at the same composition: $\delta E_{\text{ord}}(\sigma) = \Delta E_{\text{CE}}(\sigma) - \Delta E_{\text{CE}}(\text{rand}, x)$. Assuming ideal mixing entropy (IME), T_c can be estimated from $\delta E_{\text{ord}} \approx kT_c^{\text{IME}}[x \ln x + (1 - x) \ln(1 - x)]$. This leads to $T_c^{\text{IME}} \approx 956$ K for Cu_3Pd in the random to LPS $\langle 4 \rangle$ transition, which is compared to the Monte Carlo simulated annealing value of $T_c^{\text{MC}} \sim 850$ K. Table VI also gives the estimated transition temperature at other composition using the IME formula.

Table VII gives a breakdown of the energies of random and ordered structures at $x = \frac{1}{4}$, $\frac{1}{2}$, and $\frac{3}{4}$ according to Eq. (25). We see that the first term—the null and point cluster energy $J_0 + J_1(2x - 1)$ does not distinguish ran-

dom from ordered structures at the same x and gives a significant asymmetry with respect to $x = \frac{1}{2}$ —is negative for both systems and dominates ΔE in Cu-Pd. The second term of Eq. (25) [also, the first term of Eq. (6)] is the total energy due to pair interactions, which in Table VII is symmetric about $x = \frac{1}{2}$. The third term denotes the contributions from many-atom interactions which is seen to be significant compared with the pair energy (it is neglected in the generalized perturbation method²⁶). Finally, the last term of Eq. (25) is the positive-definite direction-dependent constituent strain energy which is lower in these ordered structures than in the random alloy. What sets Cu-Pd and GaP-InP apart is the relative importance of the the constituent strain energy: For GaP-InP, the constituent strain energies overwhelm the other terms, so that $\Delta H > 0$. On the other hand, while for Cu-Pd, the constituent strain energies are close to those in GaP-InP, the dominant, chemically attractive

TABLE VII. The table gives the cluster expanded energies of the ordered compound and random alloy decomposed according to Eq. (25): the null and point energy, the pair energy, many-body energy, and constituent strain energy. We also give the ordering energies of the ordered structures. Energy is in units of meV/atom.

	$x = 0.25$		$x = 0.50$		$x = 0.75$	
	$\text{Cu}_{1-x}\text{Pd}_x$					
	$L1_2$	Random	$L1_0$	Random	$L1_2$	Random
$J_0 + J_1(2x - 1)$	-107.7	-107.7	-100.4	-100.4	-93.1	-93.1
Pair	21.5	27.9	-8.6	0.0	21.5	27.9
Many-body	-18.1	1.3	9.4	0.0	8.5	-2.4
Constituent strain	18.4	36.7	17.4	33.3	10.1	23.6
Total	-85.9	-41.8	-82.2	-67.1	-53.0	-44.0
δE_{ord}	-44.1		-15.1		-9.0	
	$\text{Ga}_{1-x}\text{In}_x\text{P}$					
	DO_{22}	Random	“40”	Random	DO_{22}	Random
$J_0 + J_1(2x - 1)$	-7.8	-7.8	-9.3	-9.3	-10.8	-10.8
Pair	-1.0	2.3	-11.4	0.0	-1.0	2.3
Many-body	1.5	-0.4	0.0	0.0	-1.5	0.4
Constituent strain	19.1	21.3	28.2	29.3	20.3	22.7
Total	11.8	15.4	7.5	20.0	7.0	14.6
δE_{ord}	-3.6		-12.5		-7.6	

$J_0 + J_1(2x - 1)$ term overwhelms the constituent strain energies and favors ordering ($\Delta H < 0$).

Table VII illustrates an interesting point about GaP-InP (and indeed in most alloys of zinc-blende semiconductors^{8,11,12,64,65}): Although $\Delta H > 0$ (so the $T = 0$ ground state is phase separating), still the ordering energy $\delta E_{\text{ord}} < 0$ for $\sigma = DO_{22}$ and “40.” As discussed in Refs. 8, 11, 12, 64, 65, this means that those ordered structures have a lower energy than the random alloy of the same composition, yet the energy of the relaxed decomposition products (GaP at a_{GaP} plus InP at a_{InP}) is still lower. However, if the decomposition products were held at the lattice constant $a(x)$ of the homogeneous alloy (“coherent decomposition”), then the ordered structures will be stabler than these (unrelaxed) constituents. In this case (see Fig. 2 in Ref. 65) SRO will reflect ordering tendencies, as calculated in Refs. 8 and 11. If the constituents relax from $a(x)$ to their equilibrium lattice constants (“incoherent decomposition”), then SRO will exhibit segregation tendencies. Thus, coherence will produce a $\alpha(R) < 0$ or $\mathbf{k} \neq 0$ peak in $\alpha(\mathbf{k})$, while incoherence will lead to a $\alpha(R) > 0$ or $\mathbf{k} = 0$ peak in $\alpha(\mathbf{k})$.

VI. RESULTS: COHERENT SHORT-RANGE ORDER

The Warren-Cowley short-range-order parameters⁴⁴ are defined as

$$\alpha(R_{lmn}) = 1 - \frac{P^{A/B}(R_{lmn})}{x}, \quad (26)$$

where $P^{A/B}(R_{lmn})$ is the conditional probability that an A atom is at origin while a B atom is on site (lmn) for an $A_{1-x}B_x$ alloy. From this definition $\alpha(R_{000}) = 1$ (a B atom can not sit on the A origin site). All other $\alpha(R_{lmn})$ is related to the pair correlation function $\langle \bar{\Pi}(R_{lmn}) \rangle$ of Eq. (3):

$$\alpha(R_{lmn}) = \frac{\langle \bar{\Pi}(R_{lmn}) \rangle - q^2}{1 - q^2}, \quad (27)$$

where $q = 2x - 1$. For a completely random alloy $\langle \bar{\Pi} \rangle = q^2$ and $\alpha(R_{lmn}) = 0$. When there is a preference for association of unlike neighbors, $\alpha(R_{lmn})$ is negative, while when the preference is for association of like neighbors, $\alpha(R_{lmn})$ is positive. The Fourier transform of $\alpha(R_{lmn})$ is

$$\alpha(\mathbf{k}, N_R) = \sum_{lmn}^{N_R} \alpha(R_{lmn}) e^{i\mathbf{k} \cdot \mathbf{R}_{lmn}}. \quad (28)$$

$\alpha(\mathbf{k})$ can be extracted experimentally from the measured x-ray or neutron diffuse scattering intensity

$$I_{\text{SRO}}(\mathbf{k}) = x(1-x)(f_B - f_A)^2 \alpha(\mathbf{k}), \quad (29)$$

where f_A and f_B are x-ray or neutron scattering factors.

A central question surrounding the comparison of measured and calculated $\alpha(\mathbf{k})$ is the issue of truncation of the series of Eq. (28). This can be illustrated using the mea-

sured data⁶⁶ for $\text{Cu}_{0.702}\text{Pd}_{0.298}$: The measured intensities $I_{\text{expt}}(\mathbf{k})$ can be converted into $\alpha(\mathbf{k})$ using the method of Georgopoulos and Cohen⁶⁷ or of Borie and Sparks.⁶⁸ This function can then be Fourier transformed to give $\alpha(R_{lmn})$ in successive, real-space atomic shells (lmn) . Back transforming with a cutoff R_{max} [corresponding to the inclusion of N_R shells of atoms in Eq. (28)] then yields $\alpha(\mathbf{k}, N_R)$. Figure 8 shows this quantity, evaluated from the experimental data of Ohshima, Watanabe, and Harada,⁶⁶ for $N_R = 10, 20, 30,$ and 72 . We see that a splitting of the central peaks occurs after $\gtrsim 30$ atomic shells are included in the sum (surprisingly, this splitting is not seen even after $N_R = 78$ terms for the latest experiment on $\text{Cu}_{0.715}\text{Pd}_{0.285}$, by Saha, Koga, and Ohshima⁶⁹). Figure 6(b) indicates, however, that the calculated interaction energies for shell $N_R = 20$ ($R/a_0 = 3$) and beyond are extremely small and are thus difficult to be determined accurately. Figure 9 shows that a similar conclusion can be reached by plotting $J_{\text{MF}}(\mathbf{k}, N_R)$ instead of $\alpha(\mathbf{k}, N_R)$. Here, $J_{\text{MF}}(\mathbf{k}, N_R)$ is obtained from the Krivoglaz-Clapp-Moss mean-field formula^{70,71}

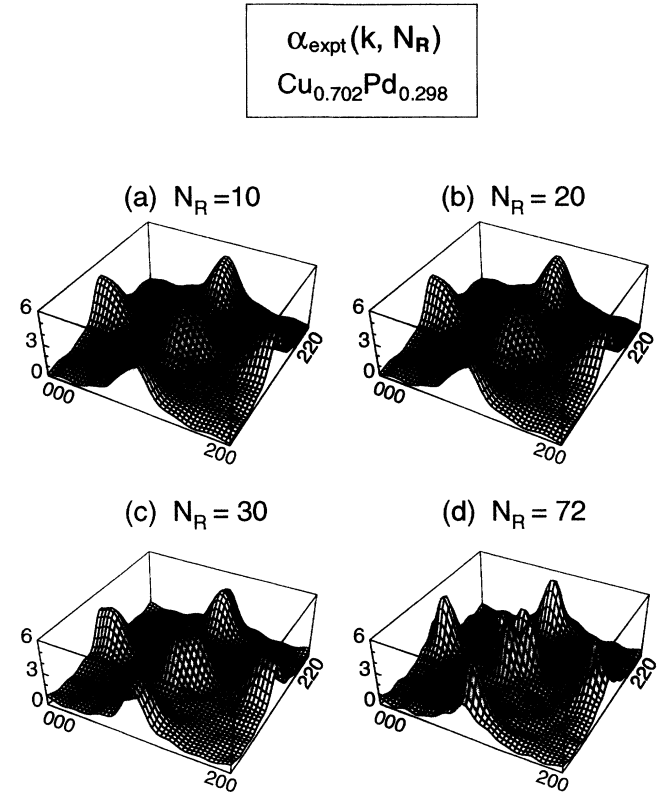


FIG. 8. This figure shows the measured (Ref. 66) reciprocal-space short-range-order maps [Eq. (27)] $\alpha(\mathbf{k}, N_R)$ as a function of the number N_R of atomic shells used for $\text{Cu}_{0.702}\text{Pd}_{0.298}$. (a) $N_R = 10$, (b) $N_R = 20$, (c) $N_R = 30$, and (d) $N_R = 72$. $\alpha(\mathbf{k}, N_R)$ was synthesized using the experimentally determined (Ref. 66) real space $\alpha(R_{lmn})$. $\alpha(R_{000})$ is taken as 1. The characteristic four-fold splitting near the $[110]$ points shows up only after $N \geq 30$ pairs are included. The plots are shown in the x - y fcc reciprocal plane, i.e., $[000]$ to $[200]_{\frac{2\pi}{a}}$ and $[000]$ to $[020]_{\frac{2\pi}{a}}$.

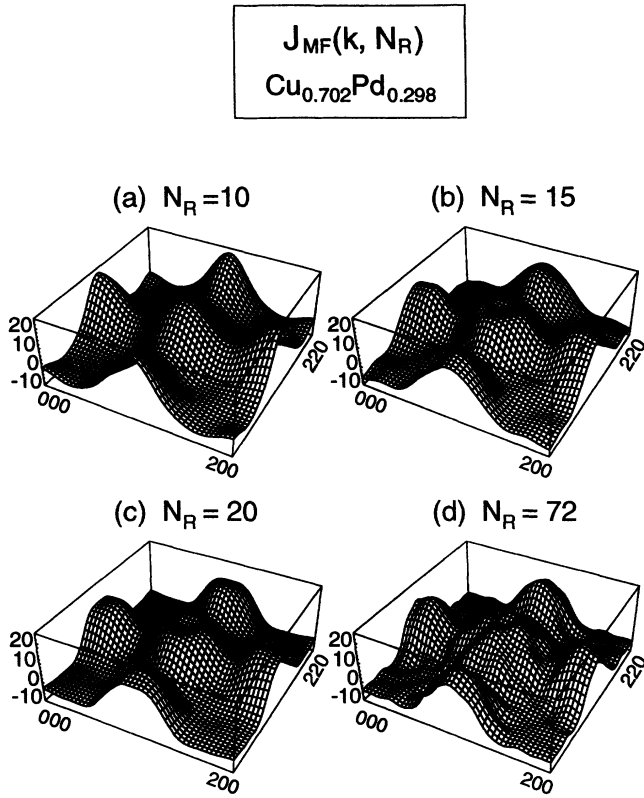


FIG. 9. This plot shows the mean-field pair interaction energies in reciprocal space $J_{MF}(\mathbf{k}, N_R)$ (in arbitrary unit) as a function of the number N_R of atomic shells used for $\text{Cu}_{0.702}\text{Pd}_{0.298}$. (a) $N_R = 10$, (b) $N_R = 15$, (c) $N_R = 20$, (d) $N = 72$. $J_{MF}(\mathbf{k}, N_R)$ was synthesized using the experimentally determined [Ref. 66] SRO parameter and the Krivoglaz-Clapp-Moss mean-field formula Eq. (30).

$$\alpha(\mathbf{k}) = \frac{1}{1 + 2x(1-x)J_{MF}(\mathbf{k})/kT}, \quad (30)$$

using for $\alpha(\mathbf{k})$ the experimental data. Again, the characteristic fourfold splitting seen in $\alpha(\mathbf{k}, N_R)$ also shows up in $J_{MF}(\mathbf{k}, N_R)$. This splitting in $J_{MF}(\mathbf{k}, N_R)$ starts to appear at $N_R \sim 15$ but is significant only past 25 shells. The splitting in $J_{MF}(\mathbf{k}, N_R)$ is much weaker than in $\alpha(\mathbf{k}, N_R)$ especially at $N_R = 72$ [see Figs. 8(d) and 9(d)]. Even though the absolute values of high order $\alpha(R_{lmn})$ are very small, their collective contributions are important in determining the appearance of split diffuse maxima. This is analogous to the situation in charge density analysis:⁷² One needs high-order structure factors $\rho(\mathbf{k})$ to accurately determine the real-space charge density $\rho(\mathbf{r})$.

A. $\alpha(R)$ for Cu-Pd

Figure 10 compares $\alpha_{\text{calc}}(R_{lmn})$ to $\alpha_{\text{expt}}(R_{lmn})$ for $\text{Cu}_{1-x}\text{Pd}_x$ for $x = 0.130, 0.285, 0.298,$ and 0.420 . The experimental data were taken from the work of Ohshima, Watanabe, and Harada⁶⁶ for $x = 0.298$ and of Saha,

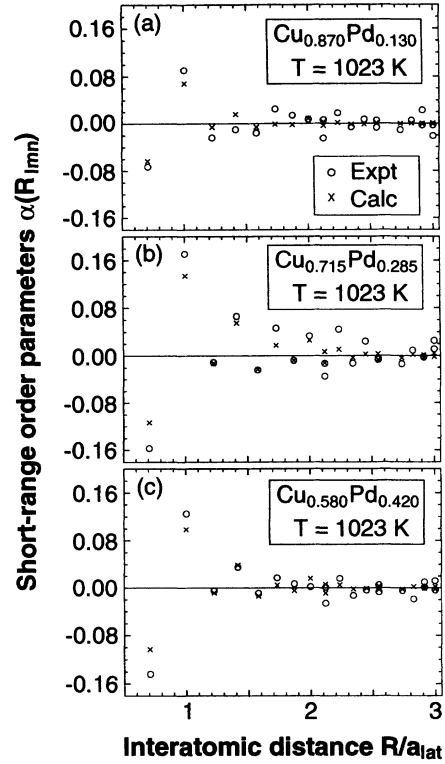


FIG. 10. Calculated real-space SRO parameters $\alpha(R_{lmn})$ (crosses) compared with measured $\alpha(R_{lmn})$ (circles) for $\text{Cu}_{1-x}\text{Pd}_x$ alloys (a) $x = 0.130$, (b) $x = 0.285$, and (c) $x = 0.420$, at $T = 1023$ K. The experimental data were taken from Ref. 69.

Koga, and Ohshima⁶⁹ for $x = 0.130, 0.285,$ and 0.420 . The measured results depend quite sensitively on the sample and preparation condition, as can be seen from Table VIII: The experimental data at $x = 0.285$ (Ref. 69), measured from a sample quenched at 1023 K, give $\alpha(R_{110}) = -0.157$. Yet, Ref. 66 finds a value that is $\sim 50\%$ different, $\alpha(R_{110}) = -0.105$, for a sample at $x = 0.298$ quenched at 773 K. [Naively, one would expect that $\alpha(R_{lmn})$ will be more negative at lower temperature, since the ordered, low-temperature phase near this composition is $L1_2$ like, for which $\alpha(R_{110}) = -\frac{1}{3}$.] By definition, $\alpha(R_{000}) = 1$; the degree of deviation from unity for the measured $\alpha(R_{000})$ reflects the quality of sample preparation, measurement, and subsequent data analyses. Thus the agreement between the theory and experiment (Fig. 10) is reasonable given the experimental scatter.

B. $\alpha(\mathbf{k})$ for Cu-Pd

Figure 1 shows how long-period superstructures (LPS's) can be constructed from $L1_2$ units. Figure 11 and Table IX show our calculated energies $E(\langle M \rangle) - E(L1_2)$ as a function of the modulation wavelength M (in units of underlying fcc lattice constant). We see that for Cu_3Pd the minimum is at $M = 3$ while in Ni_3V

TABLE VIII. Calculated and measured real-space SRO parameters $\alpha(R_{lmn})$ for $\text{Cu}_{1-x}\text{Pd}_x$ alloys.

lmn	R_{lmn}	$x = 0.130$		$x = 0.298$		$x = 0.285$			$x = 0.420$	
		$T = 1023 \text{ K}$		$T = 773 \text{ K}$	$T = 1023 \text{ K}$	$T = 1023 \text{ K}$	$T = 900 \text{ K}$	$T = 1023 \text{ K}$		
		Expt. ^a	Theory	Expt. ^b	Theory	Expt. ^a	Theory	Theory	Expt. ^a	Theory
0 0 0	0.000	1.009	1.000	1.786	1.000	1.014	1.000	1.000	1.017	1.000
1 1 0	0.707	-0.073	-0.063	-0.105	-0.116	-0.157	-0.114	-0.135	-0.144	-0.103
2 0 0	1.000	0.091	0.069	0.178	0.139	0.171	0.134	0.195	0.125	0.099
2 1 1	1.225	-0.024	-0.006	-0.028	-0.015	-0.011	-0.013	-0.027	-0.005	-0.009
2 2 0	1.414	-0.010	0.016	0.076	0.061	0.066	0.055	0.102	0.035	0.039
3 1 0	1.581	-0.016	-0.006	-0.039	-0.024	-0.024	-0.023	-0.042	-0.009	-0.014
2 2 2	1.732	0.025	-0.001	0.046	0.023	0.046	0.018	0.054	0.017	0.005
3 2 1	1.871	0.014	-0.002	-0.007	-0.009	-0.008	-0.008	-0.019	0.007	-0.005
4 0 0	2.000	0.007	0.009	0.040	0.029	0.033	0.026	0.057	0.002	0.016
3 3 0	2.121	-0.025	-0.004	-0.016	-0.013	-0.035	-0.012	-0.027	-0.026	-0.009
4 1 1	2.121	0.006	0.003	0.013	0.005	-0.013	0.007	0.006	0.001	0.006
4 2 0	2.236	0.018	0.001	0.009	0.014	0.044	0.011	0.035	0.016	0.005
3 3 2	2.345	-0.006	-0.002	-0.007	-0.005	-0.013	-0.003	-0.013	-0.013	-0.002
4 2 2	2.449	0.007	-0.001	0.000	0.006	0.024	0.002	0.021	-0.004	-0.001
4 3 1	2.550	-0.007	0.001	0.008	0.001	-0.007	0.003	0.002	0.005	0.003
5 1 0	2.550	0.005	0.000	-0.016	-0.007	-0.005	-0.007	-0.019	-0.007	-0.003
5 2 1	2.739	-0.011	0.000	-0.002	-0.004	-0.014	-0.004	-0.012	-0.005	-0.003
4 4 0	2.828	0.005	0.000	-0.007	0.005	0.009	0.002	0.013	-0.019	0.002
4 3 3	2.915	-0.003	0.000	-0.006	0.001	-0.002	0.001	0.001	0.010	0.002
5 3 0	2.915	0.023	-0.001	-0.007	-0.005	-0.003	-0.003	-0.013	0.001	-0.001
4 4 2	3.000	-0.003	-0.001	-0.006	-0.001	0.011	-0.002	0.005	-0.004	-0.003
6 0 0	3.000	-0.021	0.001	0.006	0.006	0.025	0.004	0.018	0.012	0.002

^aReference 69.^bReference 66.

and Pd_3V all superstructures are stabler than $L1_2$. In reciprocal space, the $L1_2$ structure is characterized by the X waves, while the DO_{22} structure is characterized by the fundamental wave vector $\mathbf{k} = \langle 1\frac{1}{2}0 \rangle$, i.e., the W point (it also has an X wave with smaller weight than the W wave). Had the ground state of Cu_3Pd been at $M = 1$ (DO_{22}), then by mean-field theory SRO would have peaked at the W point. This is the case for Ni_3V . However, as Fig. 11 shows, the minimum for Cu_3Pd is at $M > 1$, and so, by mean-field theory SRO will concomitantly peak *between* X and W . This is evident, in part, in Fig. 5(b) showing that $J(k)$ has a minimum *between* X and W .

Figure 12 shows calculated and measured \mathbf{k} space $\alpha(\mathbf{k}, N_R)$ for $\text{Cu}_{0.702}\text{Pd}_{0.298}$, which was Fourier synthesized using $N_R = 72$ shells of $\alpha(R_{lmn})$. The experimental result shown here is identical to Fig. 8(d). The Fourier synthesized $\alpha(\mathbf{k}, N_R)$ ($N_R = 72$) has a peak at $\langle 1k0 \rangle$ with $k = 0.18$ and a peak intensity value of 5.9. Our calculated $\alpha(\mathbf{k}, N_R)$ ($N_R = 72$ and at $T = 1023 \text{ K}$) shows the fourfold splitting with peaks at $\langle 1k0 \rangle$ ($k = 0.13$) points, i.e., between the X and W points. This peak has an intensity value of 4.3; inclusion of $N_R = 200$ terms, this peak intensity increased to a value of 5.4. Working directly in \mathbf{k} space, previous mean-field-based concentration-wave calculations²⁷ were able to show the characteristic fourfold splitting in $\alpha(\mathbf{k})$ for Cu-Pd alloys. Note that since many physical effects are ignored in this mean-field CW approach—i.e., only the “band energy” terms rather the whole LDA Hamiltonian are used (the

“charge transfer” terms are left out)—the atomic relaxation is disallowed (all bond lengths $A-A$, $A-B$, and $B-B$ are assumed equal), and it seems to be that the splitting in $\alpha(\mathbf{k})$ for Cu-Pd alloys is not sensitive to these approximations. In Ref. 27 these authors did not compare $\alpha(R)$ with experiment.

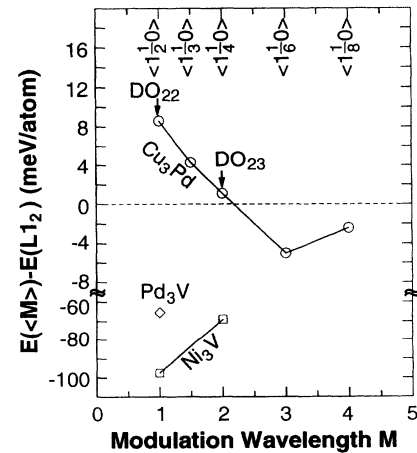


FIG. 11. This figure illustrates the LAPW-calculated formation energy of the $L1_2$ -based long-period superstructures (relative to $L1_2$ in units of meV/atom) for Cu_3Pd as a function of the modulation wavelengths M . On the top of the figure, we also give the reciprocal-space fundamental wave vectors of these LPS's. For comparison, we also show the available data of Ni_3V and Pd_3V .

TABLE IX. This table gives the LAPW-calculated and cluster-expanded (CE) formation energies of the $L1_2$ -based long-period superstructures (relative to $L1_2$ in units of meV/atom) for Cu_3Pd . For comparison, we also give the LAPW-calculated formation energies of the LPS for Ni_3V and Pd_3V .

Structure	Modulation Wavelength M	LAPW	CE	LAPW	LAPW
		Cu_3Pd		Ni_3V	Pd_3V
$L1_2$		0.0	0.0	0.0	0.0
DO_{22} ($\langle 1 \rangle$)	1.0	8.6	8.3	-105.1	-71.5
$\langle 21 \rangle$	1.5	4.3	3.5		
DO_{23} ($\langle 2 \rangle$)	2.0	1.1	0.1	-70.6	
$\langle 3 \rangle$	3.0	-5.0	-2.1		
$\langle 4 \rangle$	4.0	-2.4	-2.2		

C. $\alpha(\mathbf{R})$ and $\alpha(\mathbf{k})$ for GaP-InP: Comparison with Ni-Au

The calculated SRO for $\text{Ga}_{0.5}\text{In}_{0.5}\text{P}$ is shown in Fig. 13. The values of $\alpha(\mathbf{R}_{lmn})$ are given in Table X. Our calculated SRO of Fig. 13 is seen to peak at the $W = [1\frac{1}{2}0]$ point [corresponding to the minimum in $J(\mathbf{k})$ in Fig. 5(a)] in the BZ rather than at the $\Gamma = [000]$ point, as would be expected from the fact that the ground state corresponds to phase separation. The reason, discussed in Sec. V, is

that at a *fixed composition* the interaction energies are antiferromagnetic but the large strain that exists in this alloy favors phase separation. This was also discussed in Refs. 8 and 11. This effect has actually been observed in the $\text{Ni}_{1-x}\text{Au}_x$ alloy. The $\text{Ni}_{1-x}\text{Au}_x$ phase diagram is rather simple: It phase separates at low temperatures into Ni and Au due primarily to the large strain associated with the large ($\sim 15\%$) lattice mismatch between Ni and Au. However, the attractive chemical interaction between Ni and Au actually prefers ordering.^{30,73} Indeed,

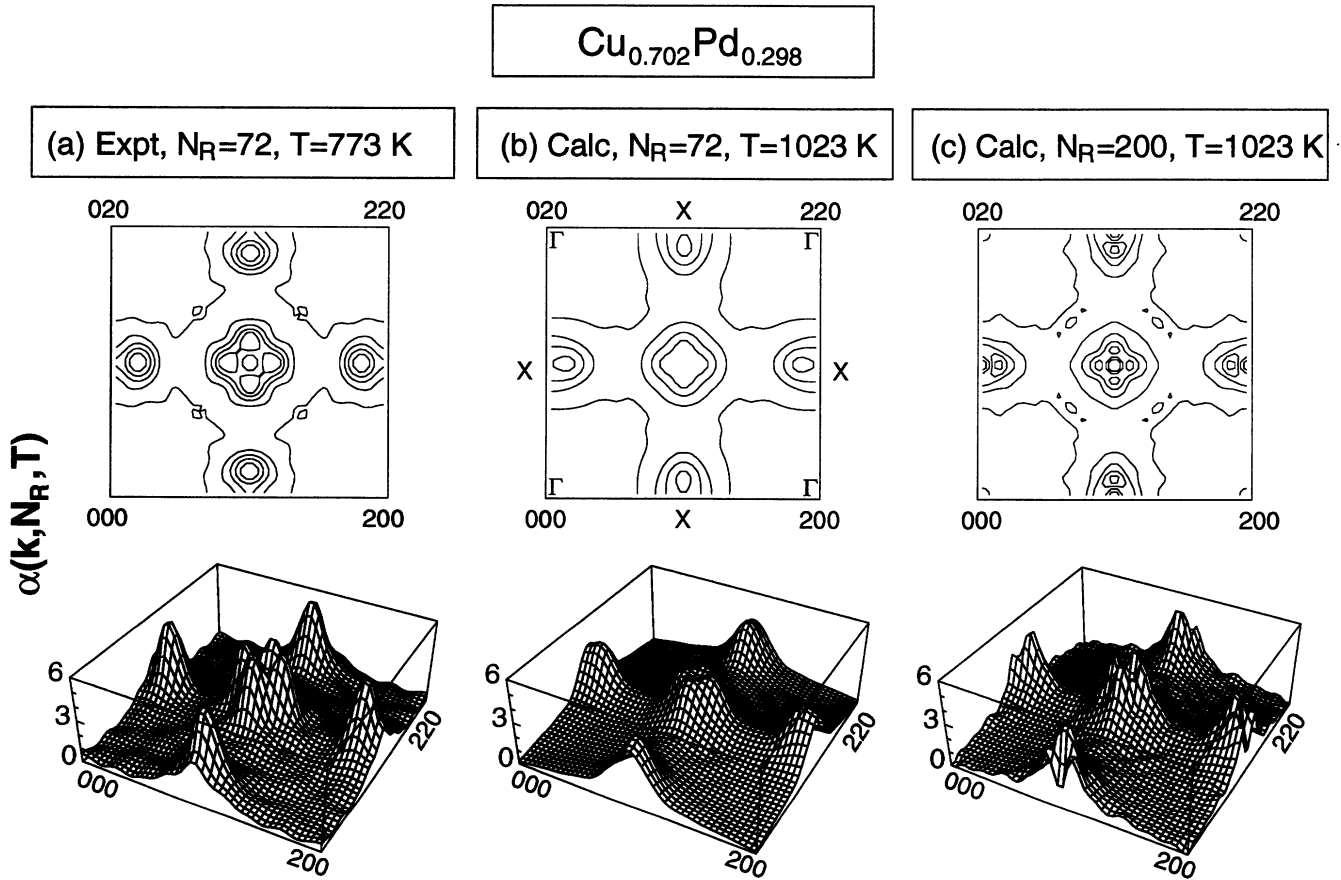


FIG. 12. Calculated and measured reciprocal SRO parameters $\alpha(\mathbf{k}, N_R, T)$ for $\text{Cu}_{0.702}\text{Pd}_{0.298}$ plotted as a contour plot (top panels) and as a three-dimensional surface plot (bottom panels). The experimental data [part (a)] was measured on a sample quenched at 773 K and fitted to $N_R = 72$ shells, while the calculations were carried out at $T = 1023$ K and the cutoff are $N_R = 72$ [part (b)] and $N_R = 200$ [part (c)].

TABLE X. Calculated real-space SRO parameters $\alpha(R_{lmn})$ for $\text{Ga}_{0.5}\text{In}_{0.5}\text{P}$ alloys.

lmn	R_{lmn}	$x = 0.5$	
		$T = 250 \text{ K}$	$T = 1200 \text{ K}$
			Theory
1 1 0	0.707	-0.122	-0.033
2 0 0	1.000	0.070	0.014
2 1 1	1.225	0.059	0.008
2 2 0	1.414	-0.066	-0.015
3 1 0	1.581	-0.017	0.003
2 2 2	1.732	-0.052	0.000
3 2 1	1.871	0.014	0.001
4 0 0	2.000	0.039	0.002
3 3 0	2.121	0.005	0.000
4 1 1	2.121	-0.007	0.001
4 2 0	2.236	0.001	-0.001
3 3 2	2.345	0.004	-0.001
4 2 2	2.449	-0.005	-0.001
4 3 1	2.550	-0.008	0.000
5 1 0	2.550	-0.005	0.001
5 2 1	2.739	0.004	0.000
4 4 0	2.828	0.015	0.000
4 3 3	2.915	-0.004	0.000
5 3 0	2.915	0.001	0.000
4 4 2	3.000	0.004	-0.001
6 0 0	3.000	0.005	0.001

this is demonstrated in an x-ray diffuse scattering experiment by Wu and Cohen⁷⁴ on a $\text{Ni}_{0.4}\text{Au}_{0.6}$ single crystal at $T = 1023 \text{ K}$. The measured short-range-order intensity has a broad peak along the Γ -X ($\langle h00 \rangle$) line, with maximum near $h_m \approx 0.6$. We extracted⁷⁵ eight $\{J\}$'s from eight LDA-calculated $\Delta E_{\text{direct}}(\sigma_s)$. We then obtain the $\alpha(R_{lmn})$ in a Monte Carlo simulation for the $\text{Ni}_{0.4}\text{Au}_{0.6}$ alloy at $T = 1500 \text{ K}$. Figure 14 shows the calculated SRO $\alpha(\mathbf{k}, N_R)$ ($N_R = 21$) for the $\text{Ni}_{0.4}\text{Au}_{0.6}$ alloy. We indeed observe the peak along the Γ -X $\langle h00 \rangle$ line, with the peak position at $h_m \approx 0.8$. Thus, in analogy with GaP-InP (indeed, with most bulk-grown semiconductor alloys) Ni-Au too shows phase separation at low temperatures, while at higher temperatures the disordered phase

exhibits ordering tendencies.

Unfortunately, most currently measured SRO parameters in GaInP^{76,77} do not lend themselves to comparison with theory since these measurements were done on *vapor-phase-grown* thin epitaxial films that are now known^{17,64,78} to exhibit *surface-induced ordering*. What is needed is SRO measurements on *melt-grown or solution-grown bulk alloys* which are closer to bulk equilibrium. Only a few results are available in this category.^{79,80} Brühl *et al.* have studied the $\text{Ga}_{1-x}\text{In}_x\text{P}$ x-ray diffuse scattering using polycrystalline samples. These samples were grown at high temperature ($> 1273 \text{ K}$), then cooled to room temperature, i.e., below the miscibility temperatures at $T \simeq 733 \text{ K}$ at $x \simeq 0.62$. These authors extracted

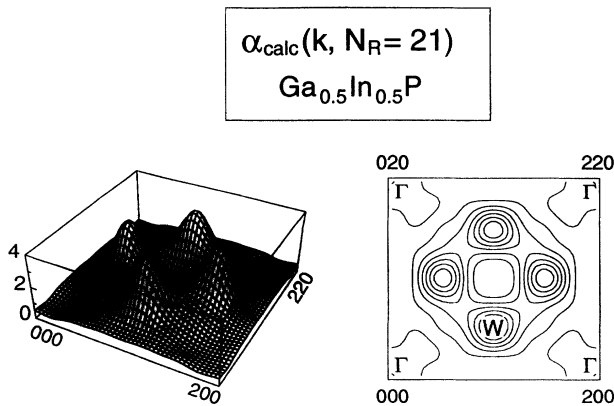


FIG. 13. Calculated reciprocal short-range-order parameters $\alpha(\mathbf{k}, N_R)$ for $\text{Ga}_{0.5}\text{In}_{0.5}\text{P}$ at $T = 250 \text{ K}$ using a cutoff of $N_R = 21$ shells.

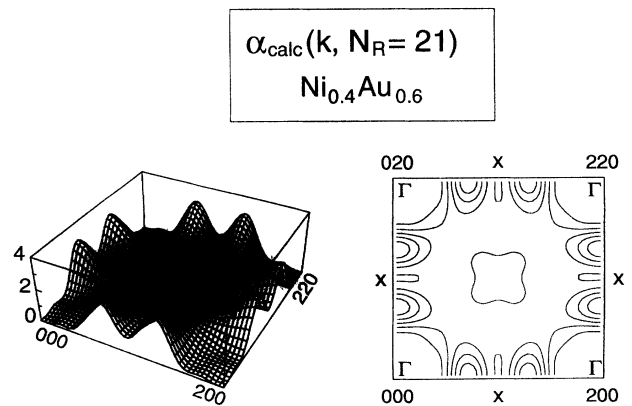


FIG. 14. Calculated reciprocal short-range-order parameters $\alpha(\mathbf{k}, N_R)$ for $\text{Ni}_{0.4}\text{Au}_{0.6}$ at $T = 1500 \text{ K}$ using a cutoff of $N_R = 21$ shells.

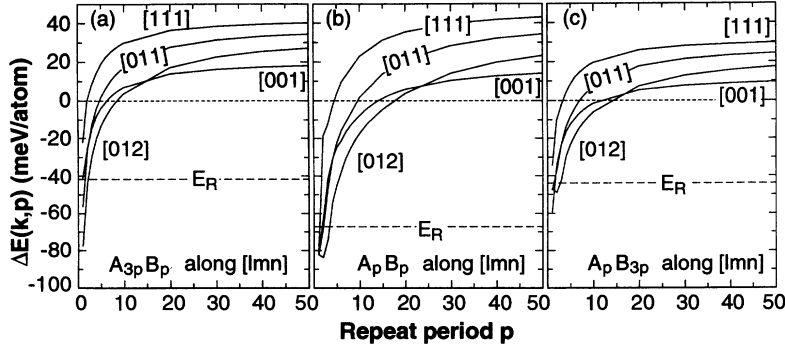


FIG. 15. The Cu_pPd_q superlattice energies as a function of repeat period. The energy E_R of the ideal random alloy is shown by the dot-dashed lines. (a) $x = \frac{1}{4}$, (b) $x = \frac{1}{2}$, and (c) $x = \frac{3}{4}$.

$\alpha(R_{110}) = +0.13$ for $x = 0.5$. The positive value reflects the fact that the sample has partly undergone a phase-segregation processes; i.e., there are local domains of GaP and InP adopting their own equilibrium volumes. More modern and accurate studies were conducted by Osamura *et al.*⁸⁰ on liquid-phase epitaxial samples of $\text{In}_{0.53}\text{Ga}_{0.47}\text{As}$, finding $\alpha(R_{110}) < 0$ and $\alpha(R_{200}) > 0$ for the first and second shells R_{110} and R_{200} , respectively, consistent with our calculated signs for GaP-InP. For more quantitative comparison, better x-ray scattering measurements are needed on bulk semiconductor alloys.

VII. SUPERLATTICE ENERGIES

As an additional application of the cluster expansion, we can predict the energies of substitutional configurations^{13,81} which are too complex to be calculated *directly* by the LDA. Once we have $\{J(\mathbf{k})\}$, $\{J_F\}$, and $\{J_{CS}\}$ we can calculate $\Delta E_{\text{CE}}(\sigma)$ of Eq. (19), since the structural function $\bar{\Pi}(\sigma)$ and $S(\mathbf{k}, \sigma)$ can be evaluated trivially using Eqs. (3) and (8), respectively. Figure 15 shows the cluster-expanded formation energies $\Delta E_{\text{CE}}(\mathbf{k}, p)$ for a Cu-Pd superlattice as a function of repeat period p . (The zero of energy, as usual, is the energy of phase-separated equilibrium Cu and Pd.) We give results for (a) $A_{3p}B_p$, (b) A_pB_p , and (c) A_pB_{3p} superlattices along four directions [001], [011], [012], and [111]. For comparison we also show as dash-dotted lines in Fig. 15 the energies E_R of the random alloys at the corresponding compositions. We see that at small repeat period p , the superlattice formation energies $\Delta E_{\text{CE}}(\mathbf{k}, p)$ are negative and lower than the random alloy values ($\delta E_{\text{ord}} < 0$), suggesting spontaneous ordering. As p increase, $\Delta E(\mathbf{k}, p)$ turns positive, and eventually approach the constituent strain energy $\Delta E_{\text{CS}}^{\text{eq}}(\mathbf{k}, x)$ limit as $p \rightarrow \infty$. The conventional truncated real-space-only cluster expansion^{8-11,25,40,81} will incorrectly predict $\Delta E(\mathbf{k}, p) = 0$ as $p \rightarrow \infty$. Note that for large periods p , the [001]-oriented superlattices are energetically the stablest, while at short period, the [012]- and [001]-oriented superlattices are energetically favorable.

Another interesting application of the CE is the stability of the one-dimensional L_{12} -based long-period superstructure in Cu_3Pd . Figure 11 shows only the LAPW-calculated excess energies for the LPS with a small num-

ber of atoms per unit cell (up to 16 atoms/cell) that are directly accessible to the first-principles method. Using the CE, we can thus extend the applicability of the first-principles method to larger unit cell, as shown in Fig. 16, where we plot the excess energy of the LPS as a function of modulation wavelength M , the cluster-expanded and LAPW-calculated excess energies are denoted by circles and squares, respectively. The excess energy has a minima around $M = 3-4$ and approaches the value of L_{12} at large modulation wavelength.

VIII. CONCLUSIONS

We have shown that LDA-calculated excess energies

$$\Delta E_{\text{direct}}(\sigma_s) = E_{\text{direct}}(\sigma_s) - [(1-x)E(A, V_A) + xE(B, V_B)]$$

of ~ 20 ordered structures σ can be used to define a converged cluster expansion

$$\Delta E_{\text{CE}} = N \sum_{\mathbf{k}} [J(\mathbf{k}) + J_{\text{CS}}(\mathbf{k})] |S(\mathbf{k}, \sigma)|^2 + N \sum_F D_F J_F \bar{\Pi}_F(\sigma)$$

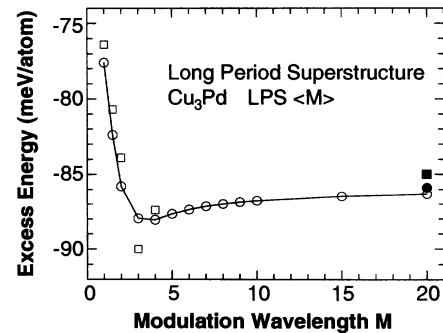


FIG. 16. The Cu_3Pd long-period superstructures (LPS $\langle M \rangle$) energies as a function of modulation wavelength M (see Fig. 1). The open circles are the cluster-expanded results, which extend the direct LAPW-calculated results (for small unit cell, denoted by the open squares) to large unit cells. The solid circle and square are the cluster-expanded and direct LAPW-calculated energies of the L_{12} structure (corresponding to LPS $\langle \infty \rangle$), respectively.

in terms of reciprocal-space pair energies $J(\mathbf{k})$, constituent strain energies $J_{CS}(\mathbf{k})$, and real-space many-body energies J_F . Once these functions are obtained from the LDA, $\Delta E_{CE}(\sigma)$ of any relaxed substitutional configuration can be obtained essentially effortlessly from structural information $S(\mathbf{k}, \sigma)$ and $\bar{\Pi}_F(\sigma)$. This cluster expansion can be readily coupled with Monte Carlo simulated-annealing methods, thus providing the $T = 0$ ground-state configurations, $T > 0$ short- and long-range order, and x versus T phase diagrams as well as prediction of internal energies of complex substitutional configurations containing thousands of transition-metal atoms. We find that use of long-range interactions is essential

to correctly predict the existence of the long-period superstructure at low temperatures and splitting in diffuse scattering intensity due to short-range order at higher temperatures for Cu_3Pd .

ACKNOWLEDGMENTS

Work at NREL was supported in part by the Office of Energy Research, Materials Science Division, U.S. DOE under Grant No. DE-AC02-83-CH10093. We also thank Dr. Ling-Wang Wang for suggesting how to speed up the Monte Carlo simulated-annealing procedure.

* Present address: Department of Physics, University of California, Davis, CA 95616.

† Present address: IBM Watson Research Center, Yorktown Heights, NY 10598.

¹ A recent review is provided by A. Zunger, in *Statics and Dynamics of Alloy Phase Transitions*, edited by P. E. A. Turchi and A. Gonis, NATO ASI Series (Kluwer, Dordrecht, 1994), p. 361.

² J. M. Sanchez, F. Ducastelle, and D. Gratias, *Physica A* **128**, 334 (1984).

³ J. Kanamori and Y. Kakehashi, *J. Phys. (Paris)* **38**, 274 (1977).

⁴ N. Metropolis *et al.*, *J. Chem. Phys.* **21**, 1087 (1953).

⁵ K. Binder and D. W. Heermann, *Monte Carlo Simulations in Statistical Physics* (Springer-Verlag, Berlin, 1988).

⁶ *The Monte Carlo Method in Condensed Matter Physics*, edited by K. Binder (Springer-Verlag, Berlin, 1992).

⁷ R. Kikuchi, *Phys. Rev.* **81**, 988 (1951).

⁸ S.-H. Wei, L. G. Ferreira, and A. Zunger, *Phys. Rev. B* **41**, 8240 (1990).

⁹ Z. W. Lu, S.-H. Wei, A. Zunger, S. Frota-Pessoa, and L. G. Ferreira, *Phys. Rev. B* **44**, 512 (1991).

¹⁰ Z. W. Lu, S.-H. Wei, A. Zunger, and L. G. Ferreira, *Solid State Commun.* **78**, 583 (1991).

¹¹ L. G. Ferreira, S.-H. Wei, and A. Zunger, *Phys. Rev. B* **40**, 3197 (1989).

¹² R. G. Dandrea, J. E. Bernard, S.-H. Wei, and A. Zunger, *Phys. Rev. Lett.* **64**, 36 (1990).

¹³ R. Magri, J. E. Bernard, and A. Zunger, *Phys. Rev. B* **43**, 1593 (1991).

¹⁴ T. Mohri, J. M. Sanchez, and D. de Fontaine, *Acta Metall.* **33**, 1463 (1985); T. Mohri, K. Terakura, S. Takizawa, and J. M. Sanchez, *ibid.* **39**, 493 (1991).

¹⁵ L. Reinhard and P. E. A. Turchi, *Phys. Rev. Lett.* **72**, 120 (1994).

¹⁶ D. B. Laks, S.-H. Wei, and A. Zunger, *Phys. Rev. Lett.* **68**, 3766 (1992).

¹⁷ R. Osório, J. E. Bernard, S. Froyen, and A. Zunger, *Phys. Rev. B* **45**, 11173 (1992).

¹⁸ D. B. Laks, L. G. Ferreira, S. Froyen, and A. Zunger, *Phys. Rev. B* **46**, 12587 (1992).

¹⁹ S. de Gironcoli, P. Giannozzi, and S. Baroni, *Phys. Rev. Lett.* **66**, 2116 (1991).

²⁰ S. V. Beiden and V. G. Vaks, *Phys. Lett. A* **163**, 209 (1992).

²¹ G. Renaud, N. Motta, F. Lancon, and M. Belakhovsky,

Phys. Rev. B **36**, 9694 (1987).

²² J. C. Mikkelsen and J. B. Boyce, *Phys. Rev. Lett.* **49**, 1412 (1982); *Phys. Rev. B* **28**, 7130 (1983); **31**, 6903 (1985).

²³ A. Balzarotti *et al.*, *Phys. Rev. B* **31**, 7526 (1985); *Solid State Commun.* **53**, 509 (1985).

²⁴ H. Dreyssé, A. Berera, L. T. Wille, and D. de Fontaine, *Phys. Rev. B* **39**, 2442 (1989).

²⁵ C. Wolverton, G. Ceder, D. de Fontaine, and H. Dreyssé, *Phys. Rev. B* **45**, 13105 (1992); **48**, 726 (1993).

²⁶ F. Ducastelle and F. Gautier, *J. Phys. F* **6**, 2039 (1976); G. Treglia, F. Ducastelle, and F. Gautier, *ibid.* **8**, 1437 (1977).

²⁷ B. L. Gyorffy and G. M. Stocks, *Phys. Rev. Lett.* **50**, 374 (1983); B. L. Gyorffy, D. D. Johnson, F. J. Pinski, D. M. Nicholson, and G. M. Stocks, in *Alloy Phase Stability*, NATO ASI Series E163, edited by G. M. Stocks and A. Gonis (Kluwer, Dordrecht, 1989), p. 421; G. M. Stocks, D. M. Nicholson, W. A. Shelton, B. L. Gyorffy, F. J. Pinski, D. D. Johnson, J. B. Staunton, B. Ginatempo, P. E. A. Turchi, and M. Sluiter, in *Statics and Dynamics of Alloy Phase Transformations*, NATO ASI Series, edited by A. Gonis and P. E. A. Turchi (Plenum, New York, 1993).

²⁸ D. D. Johnson, D. M. Nicholson, F. J. Pinski, B. L. Gyorffy, and G. M. Stocks, *Phys. Rev. Lett.* **56**, 2088 (1986).

²⁹ A. Gonis, W. H. Butler, and G. M. Stocks, *Phys. Rev. Lett.* **50**, 1482 (1983); A. Gonis, G. M. Stocks, W. H. Butler, and H. Winter, *Phys. Rev. B* **29**, 555 (1984).

³⁰ Z. W. Lu, S.-H. Wei, and A. Zunger, *Europhys. Lett.* **21**, 221 (1993).

³¹ P. P. Singh, A. Gonis, and P. E. A. Turchi, *Phys. Rev. Lett.* **71**, 1605 (1993).

³² L. G. Ferreira, A. A. Mbaye, and A. Zunger, *Phys. Rev. B* **37**, 10547 (1988).

³³ Z. W. Lu, S.-H. Wei, and A. Zunger, *Phys. Rev. B* **44**, 3387 (1991); **45**, 10314 (1992).

³⁴ S. Froyen, S.-H. Wei, and A. Zunger, *Phys. Rev. B* **38**, 10124 (1988); A. Zunger and D. M. Wood, *J. Cryst. Growth* **98**, 1 (1989).

³⁵ S.-H. Wei, A. A. Mbaye, L. G. Ferreira, and A. Zunger, *Phys. Rev. B* **36**, 4163 (1987).

³⁶ A. Carlson, *Phys. Rev. B* **35**, 4858 (1987).

³⁷ M. Sluiter and P. E. A. Turchi, *Phys. Rev. B* **40**, 11215 (1989); M. Sluiter, D. de Fontaine, X. Q. Guo, R. Podloucky, and A. J. Freeman, in *High-Temperature Ordered Intermetallic Alloys III*, edited by C. T. Liu, A. I. Taub, N. S. Stoloff, and C. C. Koch, MRS Symposia Proceedings No. 133 (Materials Research Society, Pittsburgh, PA,

- 1989), p. 3; Phys. Rev. B **42**, 10460 (1990).
- ³⁸ C. Amador, W. R. L. Lambrecht, M. van Schilfgaarde, and B. Segall, Phys. Rev. B **47**, 15276 (1993).
- ³⁹ C. Wolverton, D. de Fontaine, and H. Dreyssé, Phys. Rev. B **48**, 5766 (1993).
- ⁴⁰ J. W. D. Connolly and A. R. Williams, Phys. Rev. B **27**, 5169 (1983).
- ⁴¹ A. G. Khachaturyan, *Theory of Structural Transformations in Solids* (Wiley, New York, 1983), p. 459.
- ⁴² P. Hohenberg and W. Kohn, Phys. Rev. **136**, B864 (1964); W. Kohn and L. J. Sham, *ibid.* **140**, A1133 (1965).
- ⁴³ S. Kirkpatrick, C. D. Gelatt, Jr., and M. P. Vecchi, Science **220**, 671 (1983).
- ⁴⁴ J. M. Cowley, J. Appl. Phys. **21**, 24 (1950).
- ⁴⁵ L. Guttman, in *Solid State Physics*, edited by F. Seitz and D. Turnbull (Academic Press, New York, 1956), Vol. 3, p. 145.
- ⁴⁶ J. L. Martins and A. Zunger, Phys. Rev. B **30**, 6127 (1984).
- ⁴⁷ A. Zunger, S.-H. Wei, L. G. Ferreira, and J. E. Bernard, Phys. Rev. Lett. **65**, 352 (1990); S.-H. Wei, L. G. Ferreira, J. E. Bernard, and A. Zunger, Phys. Rev. B **42**, 9622 (1990); S.-H. Wei and A. Zunger, *ibid.* **43**, 1662 (1991); Z. W. Lu, S.-H. Wei, and A. Zunger, *ibid.* **44**, 10470 (1991).
- ⁴⁸ M. E. Fisher and W. Selke, Phys. Rev. Lett. **44**, 1502 (1980).
- ⁴⁹ G. Ceder, D. de Fontaine, H. Dreyse, D. M. Nicholson, G. M. Stocks, and B. L. Gyorffy, Acta Metall. Mater. **38**, 2299 (1990); G. Ceder, P. Huang, S. Menon, D. de Fontaine, D. M. Nicholson, G. M. Stocks, and B. L. Gyorffy, in *Alloy Phase Stability and Design*, MRS Symposia Proceedings No. 186, edited by G. M. Stocks, D. P. Pope, and A. F. Giamei (Materials Research Society, Pittsburgh, 1991), p. 65.
- ⁵⁰ O. K. Andersen, Phys. Rev. B **12**, 3060 (1975); E. Wimmer, H. Krakauer, M. Weinert, and A. J. Freeman, *ibid.* **24**, 864 (1981); D. R. Hamann, Phys. Rev. Lett. **42**, 662 (1979); S.-H. Wei and H. Krakauer, *ibid.* **55**, 1200 (1985); S.-H. Wei, H. Krakauer, and M. Weinert, Phys. Rev. B **32**, 7792 (1985).
- ⁵¹ E. Wigner, Phys. Rev. **46**, 1002 (1934).
- ⁵² D. M. Ceperley and B. J. Alder, Phys. Rev. Lett. **45**, 566 (1980).
- ⁵³ J. P. Perdew and A. Zunger, Phys. Rev. B **23**, 5048 (1981).
- ⁵⁴ H. J. Monkhorst and J. D. Pack, Phys. Rev. B **13**, 5188 (1976).
- ⁵⁵ R. Yu, D. J. Singh, and H. Krakauer, Phys. Rev. B **43**, 6411 (1991).
- ⁵⁶ K. Ishida, T. Nomura, H. Tokunga, H. Ohitani, and T. Nishizawa, J. Less-Common Met. **155**, 193 (1989).
- ⁵⁷ P. R. Subramanian and D. E. Laughlin, J. Phase Equilibria **12**, 231 (1991).
- ⁵⁸ F. Ducastelle, *Order and Phase Stability in Alloys* (North-Holland, Amsterdam, 1991).
- ⁵⁹ G. Ceder, Ph.D. thesis, University of California at Berkeley, 1991 (unpublished).
- ⁶⁰ A. Finel and F. Ducastelle, in *Phase Transformation in Solids*, edited by T. Tsakalakos, MRS Symposia Proceedings No. 21 (Materials Research Society, Pittsburgh, 1984), p. 293.
- ⁶¹ D. Broddin, G. Van Tendeloo, J. Van Landuyt, S. Amelinckx, and A. Loiseau, Philos. Mag. B **57**, 31 (1988); D. Broddin, G. Van Tendeloo, J. Van Landuyt, and S. Amelinck, Philos. Mag. A **59**, 47 (1989); D. Broddin, G. Van Tendeloo, and S. Amelinck, in *Alloy Phase Stability*, edited by G. M. Stocks and A. Gonis (Kluwer, Dordrecht, 1989), p. 113.
- ⁶² S. Takeda, J. Kulik, and D. de Fontaine, J. Phys. F **18**, 1387 (1988).
- ⁶³ J. Planès, A. Loiseau, and F. Ducastelle, J. Phys. I France **2**, 1507 (1992).
- ⁶⁴ A. Zunger and S. Mahajan, in *Handbook of Semiconductors*, 2nd ed., edited by S. Mahajan (Elsevier, Amsterdam, 1994), Vol. 3.
- ⁶⁵ J. E. Bernard, L. G. Ferreira, S.-H. Wei, and A. Zunger, Phys. Rev. B **38**, 6338 (1988).
- ⁶⁶ K. Ohshima, D. Watanabe, and J. Harada, Acta Crystallogr. A **32**, 883 (1976).
- ⁶⁷ P. Georgopoulos and J. B. Cohen, J. Phys. (Paris) Colloq. **38**, C7-191 (1977).
- ⁶⁸ B. Borie and C. J. Sparks, Acta Crystallogr. A **27**, 198 (1971).
- ⁶⁹ D. K. Saha, K. Koga, and K. Ohshima, J. Phys. Condens. Matter **4**, 10093 (1992).
- ⁷⁰ M. A. Krivoglaz, *Theory of X-Ray and Thermal Neutron Scattering by Real Crystals* (Plenum, New York, 1969).
- ⁷¹ P. C. Clapp and S. C. Moss, Phys. Rev. **142**, 418 (1966); *ibid.* **171**, 754 (1968); S. C. Moss and P. C. Clapp, *ibid.* **171**, 764 (1968).
- ⁷² Z. W. Lu and A. Zunger, Acta Crystallogr. A **48**, 545 (1992); Z. W. Lu, S.-H. Wei, and A. Zunger, Acta Metall. Mater. **40**, 2155 (1992); Z. W. Lu, A. Zunger, and M. Deutsch, Phys. Rev. B **47**, 9385 (1993); Z. W. Lu, A. Zunger, and A. G. Fox, Acta Metall. Mater. (to be published).
- ⁷³ P. A. Flinn, B. L. Averbach, and M. Cohen, Acta Metall. **1**, 664 (1953).
- ⁷⁴ T. B. Wu and J. B. Cohen, Acta Metall. **31**, 1929 (1983).
- ⁷⁵ Z. W. Lu and A. Zunger, Phys. Rev. B (to be published).
- ⁷⁶ S. Yasuami, C. Nozaki, and Y. Ohba, Appl. Phys. Lett. **52**, 2031 (1988).
- ⁷⁷ S. Yasuami, K. Koga, K. Ohshima, S. Sasaki, and M. Ando, J. Appl. Crystallogr. **25**, 514 (1992).
- ⁷⁸ S. Froyen and A. Zunger, Phys. Rev. Lett. **66**, 2132 (1991); J. Bernard, S. Froyen, and A. Zunger, Phys. Rev. B **44**, 11178 (1991).
- ⁷⁹ H.-G. Brühl, L. Hildisch, H. Morwinski, W. Schmidt, and E. Schubert, Phys. Status Solidi A **39**, 133 (1977).
- ⁸⁰ K. Osamura, M. Sugahara, and K. Nakajima, Jpn. J. Appl. Phys. **26**, L-1746 (1987).
- ⁸¹ M. Sluiter and P. E. A. Turchi, Phys. Rev. B **46**, 2565 (1992).

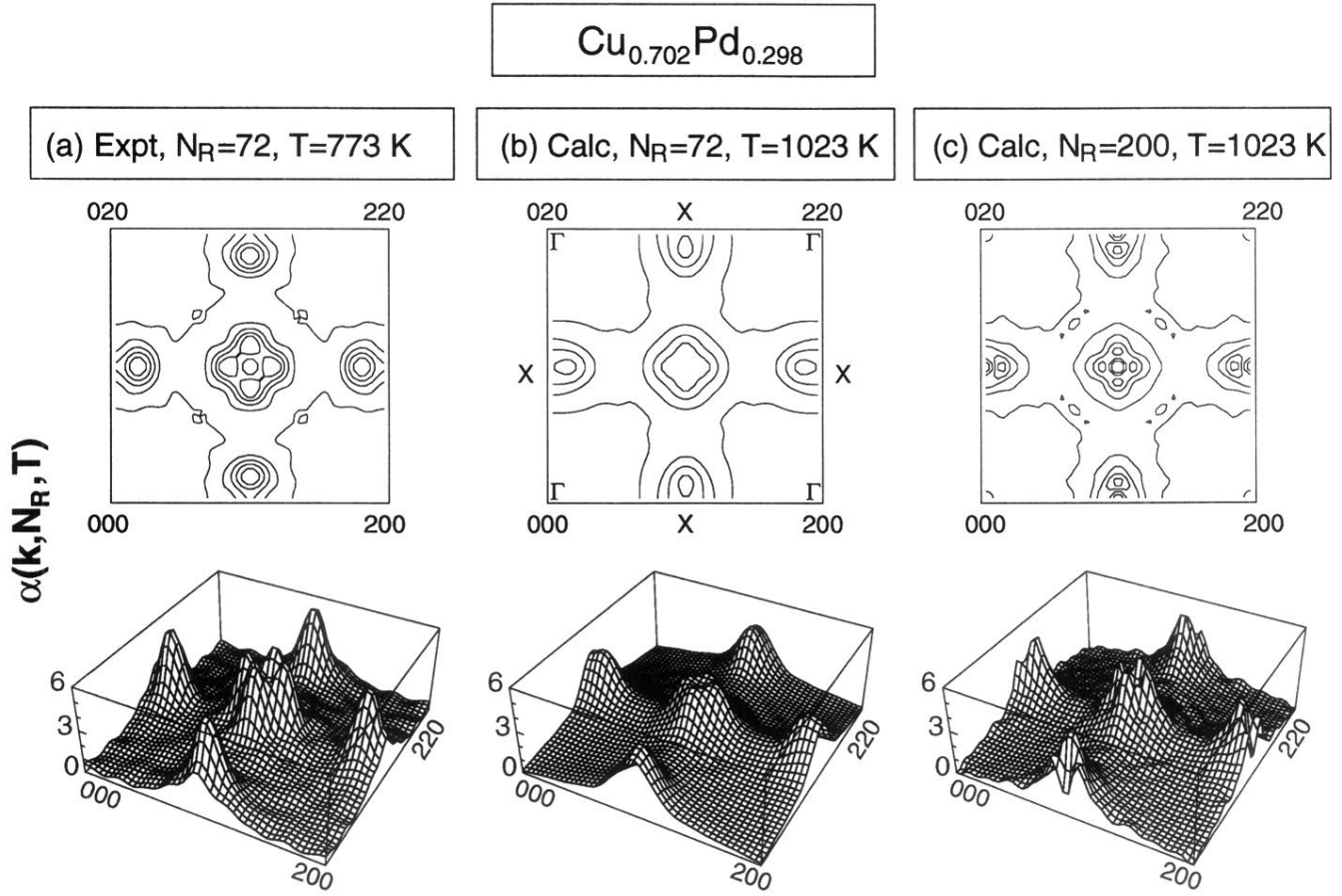


FIG. 12. Calculated and measured reciprocal SRO parameters $\alpha(\mathbf{k}, N_R, T)$ for $\text{Cu}_{0.702}\text{Pd}_{0.298}$ plotted as a contour plot (top panels) and as a three-dimensional surface plot (bottom panels). The experimental data [part (a)] was measured on a sample quenched at 773 K and fitted to $N_R = 72$ shells, while the calculations were carried out at $T = 1023$ K and the cutoff are $N_R = 72$ [part (b)] and $N_R = 200$ [part (c)].

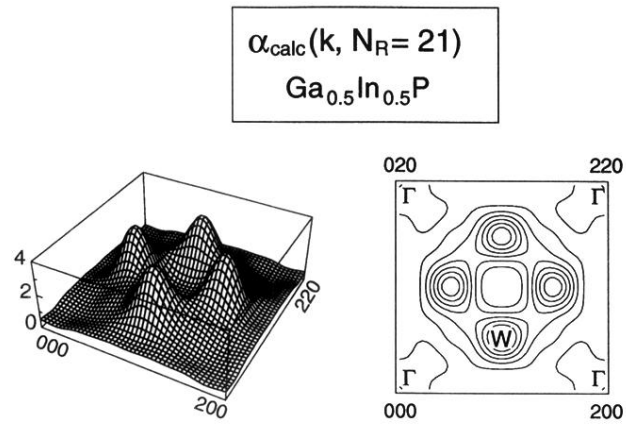


FIG. 13. Calculated reciprocal short-range-order parameters $\alpha(\mathbf{k}, N_R)$ for $\text{Ga}_{0.5}\text{In}_{0.5}\text{P}$ at $T = 250$ K using a cutoff of $N_R = 21$ shells.

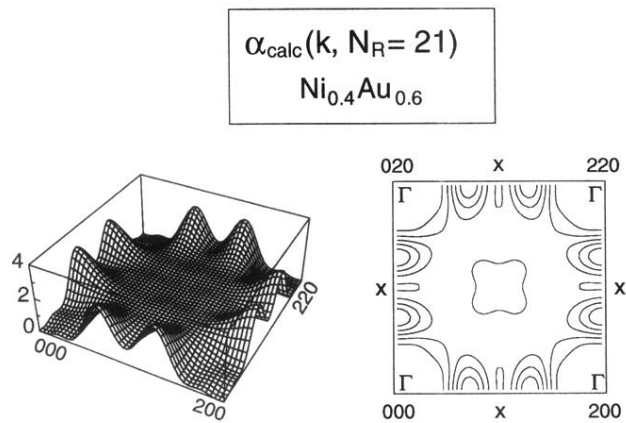


FIG. 14. Calculated reciprocal short-range-order parameters $\alpha(\mathbf{k}, N_R)$ for $\text{Ni}_{0.4}\text{Au}_{0.6}$ at $T = 1500$ K using a cutoff of $N_R = 21$ shells.

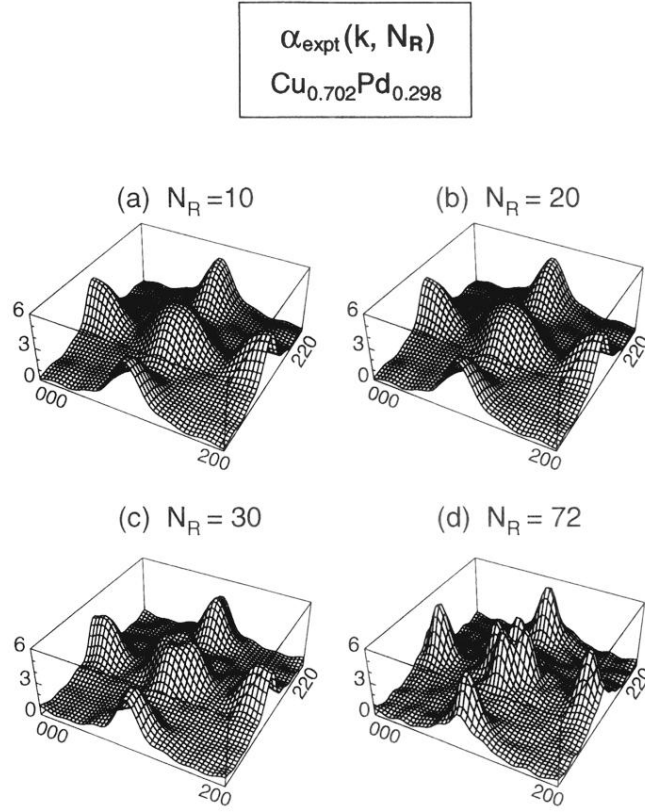


FIG. 8. This figure shows the measured (Ref. 66) reciprocal-space short-range-order maps [Eq. (27)] $\alpha(\mathbf{k}, N_R)$ as a function of the number N_R of atomic shells used for $\text{Cu}_{0.702}\text{Pd}_{0.298}$. (a) $N_R = 10$, (b) $N_R = 20$, (c) $N_R = 30$, and (d) $N_R = 72$. $\alpha(\mathbf{k}, N_R)$ was synthesized using the experimentally determined (Ref. 66) real space $\alpha(R_{lmn})$. $\alpha(R_{000})$ is taken as 1. The characteristic four-fold splitting near the $[110]$ points shows up only after $N \geq 30$ pairs are included. The plots are shown in the x - y fcc reciprocal plane, i.e., $[000]$ to $[200]\frac{2\pi}{a}$ and $[000]$ to $[020]\frac{2\pi}{a}$.

$$J_{MF}(\mathbf{k}, N_R)$$

$$\text{Cu}_{0.702}\text{Pd}_{0.298}$$

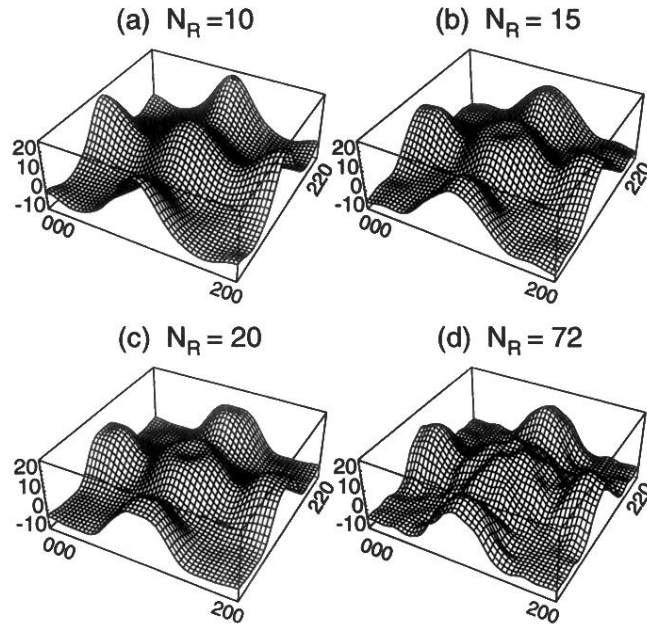


FIG. 9. This plot shows the mean-field pair interaction energies in reciprocal space $J_{MF}(\mathbf{k}, N_R)$ (in arbitrary unit) as a function of the number N_R of atomic shells used for $\text{Cu}_{0.702}\text{Pd}_{0.298}$. (a) $N_R = 10$, (b) $N_R = 15$, (c) $N_R = 20$, (d) $N = 72$. $J_{MF}(\mathbf{k}, N_R)$ was synthesized using the experimentally determined [Ref. 66] SRO parameter and the Krivoglaz-Clapp-Moss mean-field formula Eq. (30).